arXiv:1010.2409v1 [astro-ph.HE] 12 Oct 2010

Chandra High Resolution Spectroscopy of the Circumnuclear Matter in the Broad Line Radio Galaxy, 3C 445

J. N. Reeves

Astrophysics Group, School of Physical & Geographical Sciences, Keele University, Keele, Staffordshire ST5 5BG, UK; e-mail jnr@astro.keele.ac.uk

CSST, University of Maryland Baltimore County, 1000 Hilltop Circle, Baltimore, MD 21250, USA

J. Gofford

Astrophysics Group, School of Physical & Geographical Sciences, Keele University, Keele, Staffordshire ST5 5BG, UK

V. Braito

University of Leicester, Department of Physics & Astronomy, University Road, Leicester LE1 7RH, UK

R. Sambruna

Code 662, NASA Goddard Space Flight Center, Greenbelt, MD 20771, USA

ABSTRACT

We present evidence for X-ray line emitting and absorbing gas in the nucleus of the Broad-Line Radio Galaxy (BLRG), 3C 445. A 200 ks Chandra LETG observation of 3C 445 reveals the presence of several highly ionized emission lines in the soft X-ray spectrum, primarily from the He and H-like ions of O, Ne, Mg and Si. Radiative recombination emission is detected from O VII and O VIII, indicating that the emitting gas is photoionized. The He-like emission appears to be resolved into forbidden and intercombination line components, which implies a high density of $> 10^{10}\,\mathrm{cm}^{-3}$, while the Oxygen lines are velocity broadened with a mean width of $\sim 2600\,\mathrm{km\,s}^{-1}$ (FWHM). The density and widths of the ionized lines indicate an origin of the gas on sub-parsec scales in the Broad Line Region (BLR). The X-ray continuum of 3C 445 is heavily obscured either by a partial coverer or by a photoionized absorber of column density $N_{\mathrm{H}} = 2 \times 10^{23}\,\mathrm{cm}^{-2}$ and ionization parameter $\log\xi = 1.4\,\mathrm{erg\,cm\,s}^{-1}$. However the view of the X-ray line emission is unobscured, which requires the absorber to be located at radii well within any parsec scale molecular torus. Instead we suggest that the X-ray absorber in 3C 445 may be associated with an outflowing, but clumpy accretion disk wind, with an observed outflow velocity of $\sim 10000\,\mathrm{km\,s^{-1}}$.

Subject headings: Galaxies: active — galaxies: individual (3C 445)— X-rays: galaxies

1. Introduction

The X-ray emission from AGN is a powerful tool to investigate the structure and physical conditions of the matter in the proximity of the central supermassive black hole. Sensitive X-ray spectroscopy has been very successful in disentangling the contributions from warm and cold matter in AGN; e.g. see Turner & Miller (2009) for a review. At soft X-ray energies more than 50% of nearby Seyfert 1s exhibit complex intrinsic absorption and/or emission lines suggesting the presence of photoionized gas (Crenshaw et al. 2003; Blustin et al. 2005; McKernan et al. 2007), which may contain a significant fraction of the accreting mass. This is observed in the form of X-ray absorption in type 1 AGN, otherwise known as "warm absorbers", which have typical outflow velocities in the UV and X-ray band of $100–1000\,\mathrm{km\,s^{-1}}$ (Crenshaw et al. 2003). The same absorbing gas is thought to be responsible for the soft X-ray emission lines observed in type-2 sources (Guainazzi & Bianchi 2007; Kinkhabwala et al. 2002; Turner et al. 1997), which may be associated with parsec scale gas, photoionized by the inner central engine. Furthermore in a handful of radio-quiet AGN, blueshifted absorption features have been observed with higher velocity shifts, through detections of resonance absorption lines in the iron K band, indicating an outflow from the nucleus with quasi–relativistic velocities, $v/c \sim 0.1$ (e.g. see Tombesi et al. 2010 and references therein).

Until very recently, the general consensus from the X-ray spectra of radio-loud AGN was that, unlike their radio-quiet cousins, they contained little or no ionized gas in their nuclei. Thus there appeared to be no evidence for ionized emitting or absorbing gas in the soft X-ray spectra of Broad Lined Radio Galaxies (BLRGs). For instance a 120 ks *Suzaku* observation of 3C 120 showed a featureless continuum at soft X-rays, attributed to the radio jet (Kataoka et al. 2007), while a featureless soft X-ray continuum was observed in 3C 390.3 (Sambruna et al. 2009).

Recent sensitive observations with *Chandra*, *XMM-Newton*, and *Suzaku* are subverting this view. Lines in emission and absorption have been detected at soft X-rays in type 1 (Broad-Line, BLRGs) and in type 2 (Narrow-Line, NLRGs) Radio Galaxies, indicating large gas column densities, of $N_{\mathrm{H}} = 10^{21} - 10^{23}\,\mathrm{cm^{-2}}$ and a range of ionization parameters,

$\log\xi \sim 1 - 5$ ergs cm s^{-1} (Sambruna et al. 2007, Grandi et al. 2007, Piconcelli et al. 2008, Torresi et al. 2009, Torresi et al. 2009, Reeves et al. 2009, Torresi et al. 2010, Tombesi et al. 2010b). Ionized soft X-ray emission lines have so far been detected in the BLRG 3C 445 (Sambruna et al. 2007; Grandi et al. 2007) and in the NLRGs 3C 234 (Piconcelli et al. 2008) and 3C 33 (Torresi et al. 2009). Photoionized absorption lines, consistent with gas outflowing on parsec scales with velocities of hundreds of km s^{-1}, were detected for the first time with grating resolution X-ray spectra in the BLRG 3C 382, with Chandra/HETG (Reeves et al. 2009) and independently with XMM-Newton/RGS (Torresi et al. 2010). Interestingly, Suzaku observations of BLRGs has also uncovered evidence at higher energies, at $7 - 9$ keV in the iron K band, for fast outflowing gas with velocities $v_{\rm out} \sim 0.04 - 0.15c$, carrying substantial masses and kinetic powers similar to the radio jets (Tombesi et al. 2010b). Thus there appears to be substantial ionized gas in the nuclei of radio-loud AGN, and this gas may be an energetically important component that needs to be accounted for in models for accretion and jet formation.

Indeed, there are reasons to expect the presence of such a medium in BLRGs and other radio-loud AGN. For example centrifugally-driven winds, lifting matter off the disk's surface and channelling it down the magnetic field, are a proposed scenario for the origin of relativistic jets (Blandford & Payne 1982); at favorable orientations, these winds lead to observable discrete absorption/emission features at soft X-rays (Königl & Kartje 1994). Jet formation models predict that the relativistically moving plasma should be enveloped in a sub-relativistic wind (McKinney 2006), with velocities $\lesssim 0.1c$. Unification models for radio-loud sources also postulate the presence of a warm, scattering gas to explain type-2 sources (Antonucci 1993; Urry & Padovani 1995).

1.1. The Broad Lined Radio Galaxy 3C 445

3C 445 is a bright, nearby ($z = 0.0562$, Hewitt & Burbidge 1991; Eracleous & Halpern 2004) and luminous ($L_{\rm bol} \sim 10^{45}$ erg s^{-1}, Marchesini et al. 2004) radio galaxy with an FRII morphology (Kronberg 1986). 3C 445 appears lobe rather than core dominated (Morganti et al. 1993) and is likely to be highly inclined with respect to the radio-jet axis, with an inclination angle of $\sim 60 - 70°$ (Eracleous & Halpern 1998; Sambruna et al. 2007). Based on its optical spectra it is classed as a BLRG, due to the presence of strong broad permitted lines in unpolarized light (Osterbrock et al. 1976; Crenshaw et al. 1988, Eracleous & Halpern 1994; Corbett et al. 1998). From its rather large Balmer decrement, the line of sight reddening towards 3C 445 is $E_{B-V} \sim 1$, which for a Galactic dust to gas ratio suggests an absorbing column density of $N_{\rm H} \sim 5 \times 10^{21}$ cm^{-2}, an order of magnitude higher than the Galactic line of sight column (Dickey & Lockman 1990).

3C 445 is also a bright source in the X-ray band, having previously been detected by EXOSAT (Turner & Pounds 1989), Ginga (Pounds 1990), ASCA (Sambruna et al. 1998) and is also detected in the hard X-ray band (above 10 keV), with Beppo-SAX (Grandi et al. 2006), Swift/BAT (Tueller et al. 2010) and most recently with Suzaku (Braito et al. 2010). Past observations with EXOSAT, Ginga and ASCA all indicated an absorbed X-ray spectrum, with a column density of $N_{\rm H} \sim 10^{23}\,{\rm cm}^{-2}$, far in excess of the column density expected from the amount of reddening in the optical spectra of 3C 445. A more recent short (15 ks) XMM-Newton observation of 3C 445 confirmed the absorbed nature of its X-ray emission, with the absorber either partially covering the AGN, or consisting of partially ionized material (Sambruna et al. 2007; Grandi et al. 2007).

Most interestingly, the XMM-Newton observations suggested the presence of multiple highly ionized soft X-ray emission lines (Sambruna et al. 2007; Grandi et al. 2007), primarily from O, Mg and Si, with a spectrum somewhat reminiscent of those of Seyfert 2 galaxies (Guainazzi & Bianchi 2007). Given the relatively low exposure and lower resolution of the XMM-Newton EPIC-pn data below 2 keV, it was impossible to deduce the physical properties or location of the emitting gas, which was constrained to lie within < 5 kpc of the nucleus in 3C 445 (Sambruna et al. 2007). A tentative detection of the O VII and O VIII emission lines was made in the XMM-Newton RGS observations (Grandi et al. 2007), however the short exposure precluded a more detailed analysis of the soft X-ray line emitting gas.

In this paper we present direct evidence for the photoionized circumnuclear gas around the nucleus of 3C 445, from high resolution spectroscopy with the Chandra LETG (Low Energy Transmission Grating, Brinkman et al. 2000). In this much deeper 200 ks exposure, we resolve multiple emission lines in the soft X-ray band from the high resolution LETG data. The higher quality of the data allows us to determine the properties and location of the emitting matter, which as we will subsequently show, is most likely to be emission from highly ionized gas associated with the BLR clouds in 3C 445. The Chandra LETG spectrum also allows an accurate measurement of the properties of the absorbing gas towards 3C 445, which appears to be outflowing with respect to the rest frame of 3C 445. A subsequent paper (Braito et al. 2010, in preparation) will discuss in detail the broad–band X-ray spectrum of 3C 445 observed with Suzaku and Swift.

The organization of this paper is as follows. In § 2 we describe the *Chandra* data reduction and analysis; in § 3 the results of the spectral analysis §4 the photoionization modeling of the spectrum; Discussion and Conclusions follow in § 5 and § 6. Throughout this paper, a concordance cosmology with $\rm H_0 = 71\ km\,s^{-1}\ Mpc^{-1}$, Ω_Λ=0.73, and Ω_m=0.27 (Spergel et al. 2003) is adopted. Errors are quoted to 90% confidence for 1 parameter of interest (i.e. $\Delta\chi^2$ or $\Delta C = 2.71$). All the spectral parameters in subsequent sections are quoted in the rest–frame of 3C 445 ($z = 0.0562$) unless otherwise stated.

2. The Chandra LETG Observations

Chandra observed 3C 445 with the LETG (Low Energy Transmission Grating) for a net exposure of 198 ks between 25 September – 3 October 2009, with the ACIS-S detector in the focal plane. The zeroth order image of 3C 445 at the aim-point of ACIS-S appears unresolved. No significant source variability was found during the observations, so the time–averaged data was used. The ±1 order spectra were summed for the LETG respectively, along with their response files. The resultant summed (background subtracted) first order count rate for the LETG is $0.0318 \pm 0.0004\,\mathrm{counts\,s^{-1}}$ over the energy range 0.5–9.0 keV.

3. The Soft X-ray Spectrum of 3C 445

3.1. Initial Continuum Modeling

Initially, in order to parameterize the LETG spectrum of 3C 445 with simple continuum models, we binned the spectra to a minimum of 10 source counts per bin and apply the χ^2 statistic. The continuum of the LETG spectrum from 3C 445 can be very crudely parameterized by a broken–powerlaw model, as is shown in Figure 1. The spectrum at higher energies, above a break energy of ~ 1.4 keV (~ 9 Å) is very hard, rising with energy (decreasing wavelength) with a photon index of $\Gamma = -0.64 \pm 0.03$. Below the break, the X-ray spectrum is softer, with $\Gamma = 1.73 \pm 0.21$. This initial parameterization of the data provided a poor fit (with $\chi^2/\mathrm{dof} = 568.5/181$, null hypothesis probability $P = 1.3 \times 10^{-41}$, where dof is the number of degrees of freedom in the fit). At soft X-ray energies, there is statistically significant scatter around the continuum due to the presence of likely emission lines, while at higher energies, residuals are present in the data, most notably emission and absorption in the iron K band between 6–8 keV (~ 2 Å). The observed flux of 3C 445 from 0.5–9 keV is $8.84 \times 10^{-12}\,\mathrm{ergs\,cm^{-2}\,s^{-1}}$.

In order to provide a more physical representation of the continuum, we fit the spectrum with a photoelectric absorption model of the form $F(E) = \mathrm{wabs} \times (\mathrm{zwabs} \times \mathrm{pow1} + \mathrm{pow2})$, where pow1 represents an absorbed power–law, pow2 the unabsorbed power–law continuum (i.e. absorbed only by the Galactic column density), wabs is the local Galactic line of sight absorber (where $N_{H,Gal} = 4.6 \times 10^{20}\,\mathrm{cm^{-2}}$ for 3C 445, Dickey & Lockman 1990) and zwabs is the intrinsic absorber of column density N_H towards 3C 445, fitted in the rest–frame of the radio galaxy ($z = 0.0562$). Solar abundances are assumed (Anders & Grevesse 1989), while the neutral absorber uses cross-sections of Morrison & McCammon (1983).

The photon indices of the two power–law components in the above model are assumed to be the same, however their respective normalizations are allowed to differ. Thus the unabsorbed power–law may represent soft X-ray emission which is Thomson scattered into our line of sight, while the absorbed power–law represents the intrinsic hard X-ray emission from an accretion disk corona. An intrinsic column density of $N_{\rm H} = (12.3 \pm 1.3) \times 10^{22}\,{\rm cm}^{-2}$ is required, while the derived photon index is still rather flat ($\Gamma = 0.78 \pm 0.13$) compared to the typical values in radio–loud AGN (e.g. Sambruna et al. 1999, Reeves & Turner 2000).

The model is a statistically poor representation of the data ($\chi^2/{\rm dof} = 421.1/181$, $P = 3.2 \times 10^{-21}$); in the soft X-ray band narrow emission–like residuals are present, while at high energies significant spectral curvature is present, as well as emission and absorption in the iron K band. The spectral curvature and very hard photon index may indicate that a more complex absorber is present, which was found to be the case in the XMM-Newton spectrum of 3C 445 (Sambruna et al. 2007).

Thus instead the spectrum was parameterized by a dual absorber of the form $F(E) = {\rm wabs} \times ({\rm zwabs} \times {\rm zpcfabs} \times {\rm pow1} + {\rm pow2})$, where zpcfabs is a photoelectric absorber which partially covers our line of sight towards the source. Thus some fraction ($f_{\rm cov}$) of the primary hard X-ray power–law (pow1) is absorbed by the partial coverer, while the remaining fraction ($1 - f_{\rm cov}$) is absorbed only by the fully covering absorber (zwabs). The scattered soft X-ray power-law continuum is absorbed only by the Galactic column, as previously described. This dual–absorber provides a good description of the continuum, especially above 2 keV where the spectral curvature is no longer present in the data/model residuals. The column density of the partial coverer is then $N_{\rm H,pcov} = (3.6 \pm 0.5) \times 10^{23}\,{\rm cm}^{-2}$, with a covering fraction of $f_{\rm cov} = 0.86 \pm 0.03$, while the fully covering absorber has a lower column of $N_{\rm H} = (5.7 \pm 0.6) \times 10^{22}\,{\rm cm}^{-2}$. The ratio of the unabsorbed (scattered) to absorbed power–law continuum is lower, $f_{\rm scatt} \sim 0.01$, consistent with what is seen in other absorbed AGN (e.g. Turner et al. 1997). The power–law photon index is now much steeper, with $\Gamma = 1.84 \pm 0.04$.

Nonetheless the fit statistic is still poor ($\chi^2/{\rm dof} = 314.7/179$, $P = 1.6 \times 10^{-9}$), with several emission lines apparent below 2 keV (e.g. in the O VII-VIII band) and at Fe K. Indeed evidence for soft X-ray line emission has been previously suggested by the XMM-Newton spectra of this source (Sambruna et al. 2007; Grandi et al. 2007). Below we give a detailed description of these emission lines, utilizing the full spectral resolution of the Chandra/LETG. We return in Section 4 to discuss more physical models for both the absorber and emitter, using the photoionization code XSTAR (Kallman et al. 2004).

3.2. The Soft X-ray Emission Line Spectrum of 3C 445

To analyse the emission lines in detail, the LETG spectra were binned more finely to sample the resolution of the detector, at approximately the FWHM spectral resolution (e.g. $\Delta\lambda = 0.05$Å bins). Thus the spectral resolution is $E/\Delta E \sim 500$ (or $600\,\mathrm{km\,s^{-1}}$ FWHM) at 0.5 keV. For the fits, the C-statistic was adopted (Cash 1979) rather than χ^2, as there are fewer than 10 counts in some of the resolution bins.

The emission lines were modeled with Gaussian profiles and the best-fit partial covering continuum model was adopted from above, allowing the continuum and absorption parameters to vary. Table 1 lists the detected lines with their observed and inferred properties, and their significance as per the C-statistic. Figures 2 and 3 show the portions of the LETG spectrum containing the strongest lines, with the model overlaid. Overall the fit statistic improves considerably upon the addition of the emission lines to the continuum model, i.e. from C/dof = 720.2/444 without emission lines (rejected at $> 99.99\%$ confidence) to C/dof = 448.3/425 upon adding the emission lines (rejected at only 85% confidence).

Indeed the majority of the individual emission lines in Table 1 and are detected at high confidence, corresponding to $\Delta C > 14$, or $> 99.9\%$ significance for 2 parameters of interest (note lines detected with a lower level of confidence are noted). For instance the O VII He-α and O VIII Lyman-α lines are detected with $\Delta C > 50$. The strongest emission lines correspond to the He-like (He-α) and H-like (Lyman-α) transitions from O VII-VIII, Ne IX-X, Mg XI-XII, and Si XIII-XIV. Fluorescence lines may also be present from S I Kα and Fe I Kα at 2.3 and 6.4 keV respectively, which may originate from reflection off Compton thick matter (see Section 4.1). Most of the rest–frame energies of the emission lines are close to their expected expected lab values[1] (see Table 1), implying that the outflow velocity of the emitting gas is within $< 1000\,\mathrm{km\,s^{-1}}$.

3.2.1. *Radiative Recombination Emission*

In addition, radiative recombination continua (RRCs) are detected from both O VII and O VIII at high ($> 99.9\%$) significance. For instance the emission line detected at 700.8 ± 1.3 eV (17.71Å) corresponds to a rest frame energy of 740.1 ± 1.4 eV (16.77Å), which is consistent with the expected energy (739.3 eV) of the O VII RRC. These have been modeled with emission from recombination edges, of variable width dependent on temperature kT, rather than as Gaussians. Note that both RRCs are resolved with a width of $kT \sim 3$ eV

---

[1] Line energies and atomic data are adopted from http://physics.nist.gov.

(see Table 1), which implies a temperature of $\sim 3 \times 10^4$ K for the emitting gas. This suggests an origin in a photoionized rather than collisionally ionized (thermal) plasma, as the temperature would need to be closer to $\sim 10^7$ K to produce substantial soft X-ray line emission from collisionally ionized gas.

3.2.2. The He-Like Line Emission

The He-like lines all appear to be resolved when modeled with a single Gaussian profile (see Table 1). Thus the He-like emission may contain a blend of lines from the forbidden (f), intercombination (i) and resonance (r) transitions. Indeed the rest energy of the He-like lines is intermediate between the expected resonance and intercombination transitions; e.g. O VII at 565 eV is intermediate between 561 eV (f) and 569 eV (i). Thus the He-like emission was fitted by a blend of 2 separate emission lines, the results are reported in Table 2. This provides an acceptable parameterization of the spectrum ($C/\mathrm{dof} = 445.3/423$). The rest energies of the O VII and Ne IX lines are all consistent (within an eV) of the expected energies of the forbidden and intercombination transitions. Figures 2 and 3 show the spectrum fitted with this line model.

In all the cases the strengths of the forbidden and intercombination emission is approximately equal (see Table 2), implying a high density plasma, i.e. $n_e > 10^{10}\,\mathrm{cm}^{-3}$ (Porquet & Dubau 2000). The R ratio quantifies the ratio of the forbidden to intercombination line strengths; i.e. $R = z/(x+y)$, where z is the forbidden line and $x+y$ represents the sum of the intercombination emission. In the 3C 445 spectrum the best constraints on R arises from the O VII triplet. Allowing the ratio of the forbidden and intercombination lines to vary results in a value of $R = 0.9^{+1.1}_{-0.3}$ (at 90% confidence), which implies an electron density in the region of $n_\mathrm{e} = 10^{10} - 10^{11}\,\mathrm{cm}^{-3}$ (e.g. Figure 8, Porquet & Dubau 2000). This suggests the emission originates from matter closer in than the Narrow Line Region (NLR), a point we discuss further in Section 5.

3.2.3. Line Widths

The velocity widths of the O VII and O VIII emission lines were also determined. The O VIII Lyman-α line is resolved with a width of $\sigma = 2.0^{+1.1}_{-0.9}$ eV (see Table 1), corresponding to a FWHM width of $2100^{+1100}_{-950}\,\mathrm{km\,s}^{-1}$; the fit statistic worsens by $\Delta C = 12$ if the line width is set to zero. Note that the separation of the O VIII Lyman-α doublet has a negligible effect on the line width. Upon modeling the He-like triplet emission using two separate Gaussian lines to represent the forbidden and intercombination emission, the O VII He-α line width was also determined, giving $\sigma = 2.4^{+2.8}_{-0.8}$ eV (see Table 1), which corresponds to a FWHM width of 3000^{+3400}_{-980} km s^{-1}. Note that the line widths of the forbidden and intercombination lines were assumed to be equal to each other in the model. The fit statistic also worsened significantly ($\Delta C = +31$) when the velocity width of the O VII lines were fixed to zero. However the lines from higher Z ions were not resolved, as the LETG spectral resolution worsens with increasing energy, however the upper-limits to their widths are consistent with the values from the Oxygen lines (see Table 1 for the H-like ions and Table 2 for the He-like ions).

In order to derive the most accurate determination of the line velocity width, we assumed that the widths of the three strongest lines from O VII(f), O VII(i) and O VIII Lyman-α were identical and tied these values in the resulting model. The resolution of the LETG is also at its highest in the O band. This yielded a best-fit velocity width of $\sigma = 1120^{+430}_{-270}$ km s^{-1} (or $\sigma = 2.1^{+0.8}_{-0.5}$ eV at 561 eV), corresponding to a FWHM width of $v_{\rm FWHM} = 2600^{+1000}_{-600}$ km s^{-1}. A contour plot showing the measurement of the FWHM velocity width of the Oxygen lines is shown in Figure 4, which shows that a velocity width of zero is excluded at $> 99.99\%$ confidence (with $\Delta C = +42$).

4. Photoionization Modeling

As discussed above, the presence of strong radiative recombination continua may suggest that the soft X-ray line emission originates from a photoionized rather than collisionally ionized plasma (Kinkhabwala et al. 2002). To test this the spectrum was fitted with a collisional model, such as by the MEKAL (Kaastra & Mewe 1993) or APEC (Smith et al. 2001) codes. We used the same continuum parameterization as before, except the ionized emission lines modeled by Gaussians are replaced by emission from a collisionally ionized APEC model. A single temperature collisional model of temperature $kT = 0.24 \pm 0.04$ keV does not provide an acceptable fit to the data ($C/\mathrm{dof} = 610.5/456$) and the model is rejected at $> 99.99\%$ confidence. Figure 5 (upper panel) shows the spectrum fitted with the APEC model in the Oxygen band, the model fails to account for the O VII triplet (the resonance line is the strongest predicted line, which is not present in the actual data), while the model does not fit the recombination emission. We also investigated whether a multiple temperature collisionally ionized model or a model with non–Solar abundances further improved the fit, but this was not the case. Thus the data appear to exclude a collisionally ionized plasma for the origin of the soft X-ray emission lines.

4.1. The Soft X-ray Emitter

Thus instead we used a grid of emission models calculated by the photoionization code XSTAR v2.1 (Kallman & McCray 1982; Kallman et al. 2004) to derive the parameters of the emitter, assuming the baseline continuum described above. Solar abundances are assumed throughout (Grevesse & Sauval 1998). A turbulent velocity of $500\,\mathrm{km\,s^{-1}}$ has been used for the emission model.[2] We assumed an initial column density of $N_{\mathrm{H}} = 10^{22}\,\mathrm{cm^{-2}}$ for the emitter as this cannot be fitted directly to the data, unlike for an absorption model, as the N_{H} and total covering factor of the emitter are largely degenerate upon each other. Likely values for both the column and covering of the emitter will be discussed further in Section 5.1.2

The overall model fitted to the data is in the same form as the partial covering model described in Section 3.1, i.e. $F(E) = \mathrm{wabs} \times (\mathrm{zwabs} \times \mathrm{zpcfabs} \times \mathrm{pow1} + \mathrm{pow2} + \mathrm{xstar_{em}})$, where $\mathrm{xstar_{em}}$ represents the photoionized emission, which is absorbed only by the Galactic line of sight column. The XSTAR model does not include the fluorescent emission from S Kα and Fe Kα, which have been modeled separately with Gaussian profiles. This provides a significantly better fit to the data than the collisional model; for comparison Figure 5 (lower) shows that the XSTAR model fits the Oxygen emission lines well, especially around the O VII triplet and RRC, in contrast to the collisional model. The overall fit statistic is improved to $C/\mathrm{dof} = 529.1/450$, which is rejected only at the 90% confidence level. The best fit parameters of this XSTAR model are listed in Table 3.

The emitter was fitted by 2 zones of gas of ionization parameter of $\log\xi = 1.8^{+0.1}_{-0.3}$ and $\log\xi = 3.0 \pm 0.4$ respectively[3]. Note that a two zone model gave only a slightly better fit (by $\Delta C = 9$ for 2 parameters) than a single zone model, thus a second higher ionization emission zone is only required at the $\sim 99\%$ confidence level. There is also some tentative evidence for super–Solar abundances of Mg and Si (all other abundances are consistent with Solar), although their values in Table 2 are not well determined.

Note no outflow velocity is required for the photoionized emitter, indeed a slight redshift is found with $v_{\mathrm{out}} = +150^{+240}_{-210}\,\mathrm{km\,s^{-1}}$, although the data are consistent with zero velocity shift (compared to systemic) for the emitter. Thus the 90% confidence limit to the emitter outflow velocity is very tightly constrained to within 60 km s^{-1} of the systemic velocity of 3C 445. In comparison the emitter outflow velocity determined from the XMM-Newton/RGS data was $v_{\rm out} = -430^{+220}_{-160}$ km s^{-1} (Grandi et al. 2007).

---

[2] We have chosen a grid whereby the turbulence velocity best matches the observed velocity width from the Gaussian line fits.

[3] The ionization parameter is defined here as $\xi = L_{\mathrm{ion}}/n_{\mathrm{e}}R^2$, where L_{ion} is the ionizing luminosity from 1–1000 Rydberg, n_{e} is the electron density and R is the radial distance to the gas. The units of ξ are $\mathrm{erg\,cm\,s^{-1}}$.

Finally instead of modeling the Fe Kα line with a Gaussian, a model consisting of Compton reflection off an optically–thick photoionized slab of gas was tested. The REFLIONX[4] model was used (Ross et al. 1999; Ross & Fabian 2005), assuming Solar abundances, with the resulting fit found to be equally good compared to the fit with Gaussian fluorescent lines. The reflector was found to be low ionization, with an upper-limit of $\log \xi < 1.7$. This is not surprising given that the rest energy of the iron Kα emission (see Table 1) is close to the expected value for neutral or lowly ionized iron (i.e. Fe I-XVII). Note that no velocity broadening is required for the reflection spectrum, which is consistent with the upper–limit to the iron Kα velocity width of $\sigma < 145$ eV (or $\sigma < 6800$ km s^{-1}). Thus the reflection spectrum could be consistent with an origin in either the outer accretion disk, or a pc-scale Compton-thick torus. The properties of the reflection component are discussed in more detail in a paper describing the Suzaku and Swift spectrum and the hard X-ray emission above 10 keV (Braito et al. 2010).

4.2. The X-ray Absorber

The neutral partial covering model provides a good phenomenological description of the absorber in 3C 445, whereby part of the primary X-ray emission is heavily absorbed (by a column of gas of $N_{\rm H} > 10^{23}$ cm^{-2}) along the line of sight. However this may also approximate a scenario whereby the absorber is partially ionized and thus can be partially transparent to continuum X-rays at soft X-ray energies. Indeed the majority of Seyfert 1 spectra show such a "warm" absorber (e.g. Reynolds 1997; Blustin et al. 2005; McKernan et al. 2007). Here we are more likely to be viewing the nucleus of 3C 445 at higher inclination angles of about $60-70$ degrees, given the likely radio orientation of the system (Eracleous & Halpern 1998; Sambruna et al. 2007). Thus in 3C 445 we may be viewing the X-ray source directly down an accretion disk wind (Gallagher & Everett 2007) or perhaps through the outer edge of the putative pc-scale molecular torus (Urry & Padovani 1995).

Initially, as a simple parameterization, the iron K band absorption was fitted by a simple photoelectric edge model. The energy of the edge was found to be $E = 7.35 \pm 0.09$ keV in the rest–frame of 3C 445, with an optical depth of $\tau = 1.0 \pm 0.2$. Thus crudely parameterized in this way, the edge energy is significantly greater than the K-shell threshold energy for neutral iron at 7.11 keV, which indicates that the iron K absorber towards 3C 445 may be at least partially ionized.

---

[4] see http://heasarc.gsfc.nasa.gov/docs/xanadu/xspec/models/reflion.html

Thus the neutral partially covering absorber (the model ZPCFABS in XSPEC), as well as the neutral fully covering absorber, were instead replaced by a single photoionized absorber, in the form of a multiplicative grid of absorption models calculated by the XSTAR v2.1 code. The XSTAR model includes the detailed treatment of the iron K-shell opacity as described by Kallman et al. (2004). Solar abundances were assumed and the absorber was assumed to fully cover the line of sight to the source. Thus the overall spectral model was in the mathematical form:- $F(E)$ = wabs × [$\mathrm{xstar_{abs}}$ × (pow1 + reflionx) + pow2 + $\mathrm{xstar_{em}}$], where $\mathrm{xstar_{abs}}$ represents the multiplicative XSTAR photoionized absorber, reflionx is the Compton reflection component and pow1, pow2, $\mathrm{xstar_{em}}$ and wabs are the direct and scattered power-laws, photoionized emitter and neutral Galactic absorber respectively, as described previously.

The photoionized absorption model provides an excellent fit to the LETG spectrum, the overall fit statistic is $C/\mathrm{dof} = 498.4/450$, which is formally acceptable. In comparison the fit statistic for the neutral partial covering model is somewhat worse, with $\Delta C = +30$ for the same degrees of freedom ($C/\mathrm{dof} = 529.1/450$). Nonetheless the partial covering model cannot be rejected with a high degree of certainty, as the overall fit statistic is only excluded at 90% confidence. The difference between the two absorber models is shown in Figure 6, it can be seen the partially ionized absorber provides a better fit to the absorption in the iron K band and in particular the position and depth of the iron K absorption profile, although otherwise the fit to the data appears similar.

The parameters of the photoionized absorber model are listed in Table 3. A column density of $N_{\mathrm{H}} = (1.85^{+0.09}_{-0.11}) \times 10^{23}\,\mathrm{cm^{-2}}$ is found for the photoionized absorber, which is moderately ionized, with $\log\xi = 1.42^{+0.20}_{-0.12}$. At this ionization, iron ions in the range Fe XV-XVIII are likely to dominate the spectrum (Kallman et al. 2004), although other ions may also be present. At this ionization state, the absorber consists of a blend of resonance lines from the above ions, similar to the model spectra that are shown in Figure 13 of Kallman et al. (2004), resulting in a broad absorption trough as observed in the LETG above 7 keV. Note however that calorimeter based resolution in the iron K band would be required to resolve the absorption line structure.

Interestingly, the best fit model appears to indicate that the absorber could be outflowing compared to the systemic velocity of 3C 445, with $v_{\mathrm{out}} = -(0.034 \pm 0.002)c$ (or $v_{\mathrm{out}} = -10200 \pm 600\,\mathrm{km\,s^{-1}}$). Note a solution with zero outflow velocity is excluded at $> 99.9\%$ confidence and the fit statistic is correspondingly worse by $\Delta C = 22.3$ in this case. The apparent blueshift of the absorber is driven by the requirement to fit the absorption profile above 7 keV in the iron K band.

Figure 7 shows the overall fit statistic (C-statistic) for the absorption model, plotted against the redshift of the photoionized absorber, obtained from stepping through the absorber redshift in small increments of $\Delta z = 10^{-3}$. Note all the other parameters of the absorber (e.g. $N_{\rm H}$ and $\log \xi$) and the continuum were also allowed to vary at each increment. Thus an absorber at a redshift of $z = 0.0562$ would require no net velocity shift compared to the host galaxy of 3C 445; however an absorber redshift of $z = 0.0562$ appears to be excluded at $> 99.99\%$ confidence from the fit statistic. Indeed the best fit absorption model to the Chandra spectrum has a redshift of $z = 0.022 \pm 0.002$. An intervening absorption system at an intermediate redshift of $z = 0.022$ would appear unlikely, as this would require the whole X-ray spectrum of 3C 445 to be absorbed, rather than just the primary power-law, which cannot be the case as the soft X-ray line emission is not absorbed by the $N_{\rm H} \sim 10^{23}\,{\rm cm}^{-2}$ column of gas. Furthermore no intervening absorption systems are known at this redshift towards 3C 445. Thus the most likely scenario is that the photoionized absorber in 3C 445 is outflowing, with a net blue-shift of approximately $-10000\,{\rm km\,s}^{-1}$ with respect to the rest–frame of 3C 445.

A further more highly ionized zone of absorbing gas is not statistically required in the LETG data, however the Suzaku data may indicate the presence of such absorption at iron K, in the form of resonance absorption from Fe XXV or Fe XXVI (Braito et al. 2010), with a similar outflow velocity to that required above. Note that the Galactic ($z = 0$) absorption column is in excess of the expected value from neutral H I measurements (e.g. Dickey & Lockman 1990), which might indicate additional neutral absorption associated with the host galaxy of 3C 445.

Finally the presence of a scattered power–law component is required in the model at high confidence ($\Delta C = 56$), which is not absorbed by the high column density photoionized absorber. The fraction of the scattered to direct power–law emission is $\sim 2\%$. Thus about 2% of the direct absorbed power-law is scattered into our line of sight by free electrons in a highly ionized plasma. As we discuss below such gas may be associated with the photoionized emission region detected in the Chandra spectrum.

5. Discussion

5.1. The Properties of the Soft X-ray Emitting Gas

The high resolution Chandra LETG observation of the BLRG 3C 445 has revealed a complex X-ray spectrum of this obscured AGN, with both emission and absorption present from layers of photoionized gas. Initially we turn our attention to the properties of the soft X-ray line emitting gas. While the presence of the soft X-ray line emission has been detected in a previous observation with XMM-Newton (Sambruna et al. 2007; Grandi et al. 2007), here for the first time we detect and resolve multiple emission lines, utilizing the high spectral resolution of the Chandra LETG. Specifically the Chandra LETG observation has resolved emission lines from highly ionized gas in the soft X-ray spectrum, primarily from the He and H-like transitions of O, Ne, Mg and Si, corresponding to the most abundant elements with K-shell emission lines over the 0.5–2.0 keV band. The direct detection of radiative recombination emission from O VII and O VIII also shows that the most likely origin of the soft X-ray line emission is from photoionized emission; indeed a model including emission from a collisionally ionized gas is unable to produce an acceptable fit to the spectrum.

5.1.1. The Distance and Density of the Gas

The emission from the He-like triplets of O VII, Ne IX, Mg XI and Si XIII appear to be resolved into their respective forbidden and intercombination lines. Indeed all of the He-like lines are well modeled in this manner, e.g. O VII for example, as discussed in Sections 3 and 4, while the line energies are in agreement with the expected rest–frame energies of the forbidden and intercombination transitions. The fact that significant intercombination emission is detected suggests the density of the plasma is high.

Indeed the ratio R of the forbidden to intercombination emission is close to $R \sim 1$ (see Section 3.2.2). This sets a lower-limit on the density of the He-like emitting gas of $n_{\rm e} > 10^{10}\,{\rm cm}^{-3}$ (see Porquet & Dubau 2000, Figure 8). Thus an upper–limit of the radial distance to the emitter from central X-ray source can be estimated from the definition of the ionization parameter of the emitting gas, i.e. $R^2 = L_{\rm ion}/\xi n_{\rm e}$. Here $L_{\rm ion}$ is the ionizing luminosity from $1-1000$ Rydberg, which from the best–fit continuum parameters in Table 3, gives $L_{\rm ion} = 3 \times 10^{44}\,{\rm erg\,s}^{-1}$ for 3C 445. The ionization parameter of the He-like emitting gas is $\log \xi = 1.8\,{\rm erg\,cm\,s}^{-1}$, as measured from the XSTAR emission model (Section 4.1, Table 3), while $n_{\rm e} > 10^{10}\,{\rm cm}^{-3}$ as described above. Thus the radial distance to the emitter derived from this method is $R < 2 \times 10^{16}$ cm (or < 0.01 pc). For an estimated black hole mass of 3C 445 of $M_{\rm BH} \sim 2 \times 10^{8}\ {\rm M}_{\odot}$ (Bettoni et al. 2003; Marchesini et al. 2004), this corresponds to a radius of $\sim 1000 R_{\rm g}$[5].

Alternatively the location of the emitting gas can be estimated from the measured line widths of the O VII-VIII emission. The best fit width of the three strongest emission lines

---

[5] where $R_{\rm g} = GM/c^2$ is the gravitational radius

(namely O VII f and i and O VIII Lyman-α) is $v_{FWHM} = 2600^{+1000}_{-600}\,\mathrm{km\,s^{-1}}$ (section 3.2.3). Thus assuming Keplerian motion, $R \sim GM_{\rm BH}/v^2$, where here we define the velocity width as $v = \frac{\sqrt{3}}{2}v_{\rm FWHM}$. Thus by this estimate $R \sim 5 \times 10^{17}\,\mathrm{cm}$ (or $R \sim 0.1\,\mathrm{pc}$).

5.1.2. The Covering Factor

We now consider the possible covering factor and column density of the emitting gas. From the XSTAR code[6], the normalization (k) of the line emission component (which is proportional to the flux received by the observer) is related to the global covering fraction of a quasi-spherical shell of gas by:-

$$k = f_{\rm cov} L_{\rm ion}(10^{38})/D^2_{\rm kpc} \qquad (1)$$

where $f_{\rm cov}$ is the global covering factor of the emitter ($f_{\rm cov} = 1$ for a spherical shell covering 4π steradians), $L_{\rm ion}(10^{38})$ is the ionizing luminosity of the source in units of $10^{38}\,\mathrm{erg\,s^{-1}}$ and $D_{\rm kpc}$ is the distance to 3C 445 in units of kpc. Thus the units of k are $10^{38}\,\mathrm{erg\,s^{-1}\,kpc^{-2}}$. Note the normalization of the XSTAR emission component (or equivalently its flux) will be lower if the covering fraction of the gas is lower.

The Hubble flow distance to 3C 445 ($z = 0.0562$) is $D = 2.37 \times 10^5\,\mathrm{kpc}$ assuming $H_0 = 71\,\mathrm{km\,s^{-1}\,Mpc^{-1}}$. From the spectral fits in Section 4 (summarized in Table 3), the normalizations of the two XSTAR emission components are $k_{\rm low} = 2.4 \times 10^{-6}$ for the lower ionization gas and $k_{\rm high} = 1.2 \times 10^{-5}$ for the higher ionization gas. Thus for an ionizing luminosity of $3 \times 10^{44}\,\mathrm{erg\,s^{-1}}$, the covering fractions of the low and high ionization emission regions are 0.045 and 0.22 respectively.

Note that this calculation is for a column density of $N_{\rm H} = 10^{22}\,\mathrm{cm^{-2}}$ for the emitter, which has been assumed in the XSTAR model. For the emitter, the column density and covering factor are largely degenerate upon each other, in other words if a lower column is assumed then the covering fraction of the gas will need to be correspondingly higher to compensate, in order to reproduce the same observed emission line spectrum. Nonetheless the covering fraction cannot be $f_{\rm cov} > 1$, hence a lower limit to the column density of $N_{\rm H} > 2.2 \times 10^{21}\,\mathrm{cm^{-2}}$ is derived for the high ionization gas.

For a plausible upper limit to the column density of the emitting gas, one may consider the fraction of the observed X-ray power-law continuum that is electron scattered into our line of sight. From the best-fit model listed in Table 3, the ratio of the scattered to directly observed continuum is 0.02. Note that the presence of such a scattered component is required by the data at a high confidence level. Thus the fraction of scattered photons is equivalent to $1 - \exp(-\sigma_{\rm T} N_{\rm H}) = 0.02$, where $\sigma_{\rm T} = 6.65 \times 10^{-25}\,{\rm cm}^2$ is the Thomson cross-section. Hence the column required to reproduce the scattered power-law emission is $N_{\rm H} = 3 \times 10^{22}\,{\rm cm}^{-2}$. Note that this electron scattering zone may be associated with the highest ionization gas in the emission line region (which may be more extended than the lower ionization region), which scatters the primary X-ray continuum back into our line of sight. Such gas is indeed envisaged in AGN Unification scenarios (Antonucci 1993) and may be responsible for the broad, permitted lines seen in polarized light in the optical spectra of type 2 AGN.

---

[6] see http://heasarc.gsfc.nasa.gov/docs/software/xstar.docs/html/node94.html

The approximate mass of the emitting gas can also be estimated. The total mass of the emitter is equal to $M = 1.23 f_{\rm cov} \times 4\pi R^2 N_{\rm H} m_{\rm p}$, where the factor $\times 1.23$ arises from the Solar composition of the gas. We adopt the radius of the emitting gas derived in Section 5.1.1 from the He-like triplets, of $R \sim 0.01\,{\rm pc}$. From the possible range of column densities discussed above of $N_{\rm H} = (2 \times 10^{21} - 3 \times 10^{22})\,{\rm cm}^{-2}$, corresponding to covering fractions of between $f_{\rm cov} = 1.0 - 0.08$ respectively, then the emitter mass is only $M \sim 0.03\ {\rm M}_{\odot}$. However the mass will be considerably higher for larger R, i.e. if the larger radius of $R \sim 0.1\,{\rm pc}$ is adopted from the Keplerian width of the Oxygen lines (see Section 5.1.1), then the mass will be of the order $M \sim 3\ {\rm M}_{\odot}$.

5.1.3. Emission from an X-ray Broad Line Region?

Thus the possible radius derived for emitting gas of $R \sim 0.01 - 0.1\,{\rm pc}$, appears to be well inside the expected radii for the Narrow Line Region (i.e. pc to kpc scales) and also within the expected size-scale of putative pc-scale molecular torus. Furthermore the likely density of this gas, of $n_{\rm e} \sim 10^{10}\,{\rm cm}^{-3}$, appears much higher than what one would associate with typical NLR densities (e.g. $n_{\rm e} \sim 10^{3}\,{\rm cm}^{-3}$, Koski 1978).

Instead the range of radii and densities calculated above appear to be consistent with what is typically expected in the AGN Broad Line Region of Seyfert 1 galaxies and quasars (e.g. Wandel et al. 1999; Kaspi et al. 2000; Peterson et al. 2004). Indeed the velocity width measured here of $\sim 2600\,{\rm km\,s}^{-1}$ (FWHM) is similar to the measured Hα FWHM width for 3C 445 of $6400\,{\rm km\,s}^{-1}$ (Eracleous & Halpern 1994), or the Hβ FWHM of $3000\,{\rm km\,s}^{-1}$ (Osterbrock, Koski & Phillips 1976).

Recently, broadened soft X-ray lines were detected by Longinotti et al. (2008) during an XMM-Newton/RGS observation of the Seyfert 1 Mrk 335 during a low flux state. The

O VIII Lyman-α line was resolved with a FWHM width of $2200 \pm 750\,\mathrm{km\,s^{-1}}$, consistent with the H$\beta$ width of this Seyfert 1 (Boroson & Green 1992). From photoionization arguments, Longinotti et al. (2008) placed a limit on the radial distance to the soft X-ray emitting gas of $< 0.06\,\mathrm{pc}$, consistent with a BLR origin. A similar claim has been made by Blustin & Fabian (2009), who detected several broadened soft X-ray emission lines with a typical FWHM of $\sim 5000\,\mathrm{km\,s^{-1}}$, from a deep XMM-Newton/RGS observation of the narrow lined Seyfert 1, 1H 0707-495. Indeed there have also been several past claims of broadened soft X-ray emission lines from grating observations of Seyfert 1s, with line widths which appear to be consistent with a BLR origin (e.g. NGC 4051, Ogle et al. 2004; NGC 5548, Steenbrugge et al. 2005; Mrk 509, Smith et al. 2007; Mrk 279, Costantini et al. 2007). Thus we may be observing the same X-ray BLR emission in the BLRG 3C 445.

5.2. Absorption from an Accretion Disk Wind in 3C 445?

As has also been found from previous observations (Sambruna et al. 2007; Grandi et al. 2007), the primary X-ray continuum from 3C 445 is highly absorbed, with a column density exceeding $10^{23}\,\mathrm{cm^{-2}}$. Indeed the X-ray column observed towards 3C 445 far exceeds the expected column based on the extinction in the optical band towards of this AGN, of the order $E_{B-V} \sim 1$ (Rudy & Tokunaga 1982). Although the properties of the absorbing gas was unclear from previous shorter (and lower spectral resolution) observations, the Chandra LETG shows the absorption can be well modeled with a moderately ionized outflow, with an outflow velocity of the order $\sim 10000\,\mathrm{km\,s^{-1}}$. As we will discuss here, it appears more plausible that this absorbing gas is associated with a disk wind on smaller (sub–parsec) scales rather than with a putative molecular torus.

5.2.1. The Likely Location of the Wind

We first consider the location of the absorber. For a homogeneous radial wind, the observed column density along the line of sight is equal to:-

$$N_{\mathrm{H}} = \int_{\mathrm{R_{in}}}^{\mathrm{R_{out}}} n_{\mathrm{e}}(R) dR = \int_{\mathrm{R_{in}}}^{\mathrm{R_{out}}} \frac{L_{\mathrm{ion}}}{\xi R^2} dR = \frac{L_{\mathrm{ion}}}{\xi} \left(\frac{1}{R_{\mathrm{in}}} - \frac{1}{R_{\mathrm{out}}} \right) \qquad (2)$$

where R_{in} and R_{out} are the inner and outer radii along the line of sight through the wind. In the case where we are looking directly down a homogeneous wind towards an inner radius R_{in}, then $R_{\mathrm{out}} = \infty$ and re-arranging gives $R_{\mathrm{in}} = L_{\mathrm{ion}}/\xi N_{\mathrm{H}}$. The best fit XSTAR model of the absorber (Table 3) gives $N_{\rm H} = 2 \times 10^{23}\,{\rm cm}^{-2}$ and $\log \xi = 1.4$, thus $R_{\rm in} = 5 \times 10^{19}$ cm (or ~ 10 pc). At this radius the density of the absorbing matter is $n_{\rm e} \sim 10^{4}\,{\rm cm}^{-3}$.

Thus a radius of $\sim$ 10 pc is consistent with a wind launched from the region of the molecular torus. However this can be considered an upper-limit, if we are only viewing across the wind, or if the wind is sufficiently clumpy, as we will argue in Section 5.3 from considering the wind energetics. In this case we can define the wind thickness as $\Delta R = R_{\rm out} - R_{\rm in}$ and assuming $\Delta R/R << 1$, then re-arranging equation 2 gives:-

$$R_{\rm in} = \frac{L_{\rm ion}}{\xi N_{\rm H}} \left(\frac{\Delta R}{R}\right) \tag{3}$$

So if $\Delta R/R << 1$ then the wind can originate on much more compact scales. Indeed if the location of the X-ray absorber is on parsec scales, then this presents a problem for both the soft X-ray emission line gas and for the emission from the optical BLR. Thus the location of the absorber cannot be outside of the soft X-ray line emission region, as otherwise the emission lines would be completely obscured. This is certainly not the case from the LETG spectrum, i.e. the soft X-ray emission is absorbed by a much lower column density of $N_{\rm H} = 1.5 \times 10^{21}\,{\rm cm}^{-2}$ (see Table 3). Furthermore the emission from the optical broad line region in 3C 445 cannot be strongly obscured by the X-ray absorbing gas, given its classification as a BLRG and the observation of broad permitted lines such as Hα or Hβ in non-polarized light (Eracleous & Halpern 1994). Thus the observational evidence suggests a more compact size-scale for the X-ray absorber in 3C 445 than the pc-scale torus.

For a scenario whereby the absorber originates from a wind launched off the accretion disk by radiation pressure, we can calculate a lower bound on the launch radius from the escape velocity. The escape radius is $R_{\rm esc} = 2c^2 R_{\rm g}/v_{\rm out}^2$, where $R_{\rm g} = 3 \times 10^{13}$ cm (for $M_{\rm BH} = 2 \times 10^{8}\ {\rm M}_{\odot}$) and $v_{\rm out} = 10^{4}\,{\rm km\,s}^{-1}$. Thus for the outflow in 3C 445, $R_{\rm esc} \sim 3 \times 10^{16}$ cm (or ~ 0.01 pc). This would appear to be a more plausible radius at which the wind is viewed, as while the central X-ray continuum would be absorbed, the sight–line towards the soft X-ray emission need not be obscured. At this radius the density would be higher, $n_{\rm e} \sim 10^{10}\,{\rm cm}^{-3}$, while the gas will be substantially clumped, i.e. $\Delta R/R \sim 10^{-3}$.

Indeed such a scenario could also be consistent with the absorbing clumps or clouds partially covering the line of sight to the central X-ray emitter. In this scenario, in order for the clouds to only partially obscure the primary X-ray continuum, they would likely have to be only a few gravitational radii in size, i.e. of the order $\sim 10^{14}$ cm. If the column density through an individual cloud is $N_{\rm H} \sim 10^{23}\,{\rm cm}^{-2}$, this would require a density of $n \sim 10^{9}\,{\rm cm}^{-3}$. Given an observed ionization parameter of $\log \xi = 1.4$, this then implies a radial distance to the clouds of $\sim 10^{17}$ cm, i.e. consistent with a sub-parsec scale location.

5.3. The Wind Energetics

For a quasi–spherical radial outflow, the mass outflow rate is given by:-

$$\dot{M}_{\rm out} = 1.23 \times 4\pi b R^2 n_{\rm e} m_{\rm p} v_{\rm out} = 1.23 \times 4\pi b \left(\frac{L_{\rm ion}}{\xi}\right) m_{\rm p} v_{\rm out} \tag{4}$$

where for the absorber in 3C 445, $L_{\rm ion}/\xi = 10^{43}\,{\rm cm}^{-1}$, while b is a geometrical factor, where $b = 1$ for a homogeneous spherical outflow, but $b < 1$ for a wind covering a fraction of 4π steradian or if the matter is clumped. Thus for the absorber in 3C 445, then $\dot{M}_{\rm out} = 2.5b \times 10^{29}\,{\rm g\,s}^{-1}$ or $\dot{M}_{\rm out} = 4000b\ {\rm M}_{\odot}\,{\rm yr}^{-1}$. This seems implausibly high for $b = 1$.

For comparison we can estimate the likely accretion rate needed to power the bolometric (radiative) output of 3C 445. The (unabsorbed) 2–10 keV X-ray luminosity of 3C 445 is $L_{2-10} = 1 \times 10^{44}\,{\rm erg\,s}^{-1}$ and assuming the 2-10 keV luminosity is approximately 5% of the bolometric output (e.g. Elvis et al. 1994), then $L_{\rm bol} = 2 \times 10^{45}\,{\rm erg\,s}^{-1}$, also in agreement with the estimate of Marchesini et al. (2004). For an accretion efficiency of $\eta = 0.05$, then the accretion rate is then $\dot{M}_{\rm acc} = L_{\rm bol}/\eta c^2 \sim 1\ {\rm M}_{\odot}\,{\rm yr}^{-1}$ for 3C 445. Thus a homogeneous wind requires $\dot{M}_{\rm out} >> \dot{M}_{\rm acc}$ for 3C 445, which would rather rapidly exhaust the supply of gas towards the central AGN.

Instead we consider the outward transfer of momentum into the wind, via radiation pressure. Thus the outward momentum rate is $\dot{p} = \dot{M}_{\rm out} v_{\rm out} = L_{\rm bol}/c \sim 10^{35}\,{\rm g\,cm\,s}^{-2}$. Thus for the measured outflow velocity of $v_{\rm out} = 10^9\,{\rm cm\,s}^{-1}$, then the mass outflow rate is $\dot{M}_{\rm out} \sim 10^{26}\,{\rm g\,s}^{-1}$ (or $\sim 1\ {\rm M}_{\odot}\,{\rm yr}^{-1}$). This appears more physically realistic with $\dot{M}_{\rm out} \sim \dot{M}_{\rm acc}$ and requires a clumping factor of $b \sim 10^{-3}$, which may be the case if the absorbing clouds are located on sub–parsec scales as discussed above. Furthermore we note that the Suzaku spectrum of 3C 445 (Braito et al. 2010) may require a very high ionization zone ($\log \xi \sim 4$) of absorbing gas in addition to the moderately ionized absorber discussed here. Indeed both the low and high ionization absorption may co–exist at the same radii in a multi–phase disk–wind, with the low ionization absorber present as higher density clouds confined within the lower density and more uniform high ionization outflow (see Figure 8).

Finally we estimate the total mechanical output of the wind in 3C 445. The kinetic power is simply $\dot{E} = \dot{M}_{\rm out} v_{\rm out}^2/2 \sim 10^{47} b\,{\rm erg\,s}^{-1}$, which for $b \sim 10^{-3}$, as discussed above, implies $\dot{E} \sim 10^{44}\,{\rm erg\,s}^{-1}$, which is approximately 10% of $L_{\rm bol}$. Note that the presence of a high ionization outflow of $\log \xi \sim 4$, as implied by the Suzaku data, also suggests a similar mechanical output, but without the requirement that the absorbing gas is clumped.

5.4. The Overall Geometry of 3C 445

Given the likely high inclination of 3C 445 compared to the radio-jet axis, of the order $60 - 70^{\circ}$ (Leahy et al. 1997; Eracleous & Halpern 1998), it is plausible that we are viewing the central engine of 3C 445 at a relatively side-on orientation. The situation may be similar to that outlined in Figure 8. Thus we may be viewing through an equatorial disk-wind in 3C 445, on scales of approximately $10^{16} - 10^{17}$ cm from the central black hole. In this toy model for 3C 445, the soft X-ray emitting clouds may be lifted above the plane of the accretion disk and could be associated with the optical BLR emission, as discussed earlier. Any highly ionized gas that is present would also serve to Thomson scatter the primary absorbed X-ray continuum back into our line of sight, as is also observed in the Chandra spectrum.

The lower ionization absorbing gas viewed here may well be clumped, within a much higher ionization, but lower density medium, co-existing at a similar radius to the high ionization gas. If such high column density ($\sim 10^{23}\,\mathrm{cm}^{-2}$) but low ionization absorbing gas were located on much larger scales, e.g. with a parsec scale torus, it would be difficult to reconcile the high column density with the much lower absorbing column (of $N_{\mathrm{H}} \sim 10^{21}\,\mathrm{cm}^{-2}$), towards the soft X-ray line emitting gas, if the latter is coincident with sub-parsec BLR scales. Instead the much lower column density gas which absorbs the soft X-ray emission spectrum might instead be associated with gas on the scale of the host galaxy and would be consistent with the amount of reddening observed towards 3C 445 (Rudy & Tokunaga 1982).

Finally if the high column absorbing medium is clumped, it might be possible to observe short-timescale N_{H} variability, due to the passage of clouds along our line of sight. For instance such aborption variability is observed along the line of sight to some Seyfert galaxies, the most notable example being the intermediate type Seyfert, NGC 1365 (Risaliti et al. 2009; Maiolino et al. 2010). However no such column density variations have been apparent so far towards 3C 445, either on short timescales within the 200 ks Chandra observations, or on longer timescales, as the total column density is also consistent with previous observations, e.g. with XMM-Newton (Sambruna et al. 2007; Grandi et al. 2007). However this may simply be explained if the number of absorbing clouds is large, which would average out any variations.

6. Conclusions

We have reported upon a deep 200 ks Chandra LETG spectrum of the absorbed BLRG, 3C 445, which displays a complex X-ray spectrum. The high resolution Chandra spectrum revealed a wealth of soft X-ray emission lines from a photoionized plasma, primarily from the He and H-like transitions of O, Ne, Mg and Si. The O VII and O VIII lines are resolved, with a typical FWHM width of $\sim 2600\,\mathrm{km\,s^{-1}}$, while the ratio of forbidden to intercombination emission in the He-like triplets indicate a high electron density, of $n_{\mathrm{e}} > 10^{10}\,\mathrm{cm^{-3}}$ (Porquet & Dubau 2000). Thus the X-ray lines appear to be consistent with an origin in the optical BLR in 3C 445, located on sub-parsec scales.

The Chandra spectrum of 3C 445 is also highly absorbed and can be modeled by either partially covering or by partially ionized absorbing gas. The high column density gas may be associated with an equatorial accretion disk wind in 3C 445, observed at high inclinations with respect to the radio jet axis. Future high resolution observations of 3C 445, with calorimeter resolution in the iron K band, e.g. with Astro-H, will potentially resolve a host of absorption lines associated with the high column density absorber, enabling us to probe the kinematics of any outflowing wind to a high level of accuracy.

This research has made use of data obtained from the High Energy Astrophysics Science Archive Research Center (HEASARC), provided by NASA's Goddard Space Flight Center. R.M.S. acknowledges support from NASA through the *Suzaku* and *Chandra* programs. We would also like to thank Tahir Yaqoob for assistance with the Chandra data analysis.

REFERENCES

Anders, E., & Grevesse, N. 1989, Geochimica et Cosmochimica Acta, 53, 197

Antonucci, R. 1993, ARA&A, 31, 473

Bettoni, D., Falomo, R., Fasano, G., & Govoni, F. 2003, A&A, 399, 869

Blandford, R.D. & Payne, D.G. 1982, MNRAS, 199, 883

Blustin, A. J., Page, M. J., Fuerst, S. V., Branduardi–Raymont, G., & Ashton, C. E. 2005, A&A, 431, 111

Blustin, A. J., & Fabian, A.C. 2009, MNRAS, 399, L169

Boroson, T. A., & Green, R. F. 1992, ApJS, 80, 109

Braito, V., Reeves, J.N., Sambruna, R., & Gofford, J. 2010, ApJ, in preparation

Brinkman, A.C., et al., 2000, ApJ, 530, L111

Cash, W. 1979, ApJ, 228, 939

Costantini, E., et al. 2007, A&A, 461, 121

Corbett, E. A., Robinson, A., Axon, D. J., Young, S., & Hough, J. H. 1998, MNRAS, 296, 721

Crenshaw, D. M., Peterson, B. M., & Wagner, R. M. 1988, AJ, 96, 1208

Crenshaw, D. M., Kraemer, S. B., & George, I. M. 2003, ARA&A, 41, 117

Dickey, J. M. & Lockman, F. J. 1990, ARA&A, 28, 215

Elvis, M., Wilkes, B. J., McDowell, J .C., Green, R. F., Bechtold, J., Willner, S. P., Oey, M. S., Polomski, E., & Cutri, R. ApJS, 95, 1

Eracleous, M., & Halpern, J. P. 1994, ApJS, 90, 1

Eracleous, M., & Halpern, J. P. 1998, ApJ, 505, 577

Eracleous, M., & Halpern, J. P. 2004, ApJS, 150, 181

Gallagher, S. C., & Everett, J. E. 2007, ASPC, 373, 305

Grandi, P., Malaguti, G., & Fiocchi, M. 2006, ApJ, 642, 113

Grandi, P., Guainazzi, M., Cappi, M., & Ponti, G. 2007, MNRAS, 381, 21

Guainazzi, M., Bianchi, S. 2007, MNRAS, 374, 1290

Grevesse, N. & Sauval, A. J. 1998, Space Sci. Rev., 85, 161

Hewitt, A., & Burbidge, G. 1991, ApJS, 75, 297

Kaastra, J. S., & Mewe, R. 1993, A&AS, 97, 443

Kallman, T. R., & McCray, R. 1982, ApJS, 50, 263

Kallman, T. R., Palmeri, P., Bautista, M. A., Mendoza, C., & Krolik, J. H. 2004, ApJS, 155, 675

Kaspi, S., Smith, P. S., Netzer, H., Maoz, D., Jannuzi, B. T., & Giveon, U. 2000, ApJ, 533, 631

Kataoka, J., et al. 2007, PASJ, 59, 279

King, A. R. 2003, ApJ, 596, L27

King, A. R. 2010, MNRAS, 402, 1516

Kinkhabwala, A., Sako, M., Behar, E., Kahn, S. M., Paerels, F., Brinkman, A. C., Kaastra, J.S., Gu, M. F., & Liedahl, D. A. 2002, ApJ, 575, 732

Königl, A. & Kartje, J. A. 1994, ApJ, 434, 446

Koski, A. 1978, ApJ, 223, 56

Kronberg, P. P., Wielebinski, R., & Graham, D. A. 1986, A&A, 169, 63

Leahy, J. P., Black, A. R. S., Dennett-Thorpe, J., Hardcastle, M. J., Komissarov, S., Perley, R. A., Riley, J. M., & Scheuer, P. A. G. 1997, MNRAS, 291, 20

Longinotti, A. L., Nucita, A., Santos-Lleo, M., & Guainazzi, M. 2008, A&A, 484, 311

Maiolino, R., Risaliti, G., Salvati, M., Pietrini, P., Torricelli-Ciamponi, G., Elvis, M., Fabbiano, G., Braito, V., & Reeves, J. N. 2010, A&A, in press (arXiv:1005.3365)

Marchesini, D., Celotti, A. & Ferrarese, L. 2004, MNRAS, 351, 733

McKernan, B., Yaqoob, T., & Reynolds, C. S. 2007, ApJ, 379, 1359

McKinney, J.C. 2006, MNRAS, 368, 1561

Morganti, R., Killeen, N. E. B., & Tadhunter, C. N. 1993, MNRAS, 263, 1023

Morrison, R., & McCammon, D. 1983, ApJ, 270, 119

Ogle, P. M., Mason, K. O., Page, M. J., Salvi, N. J., Cordova, F. A., McHardy, I. M., Priedhorsky, W. C.

Osterbrock, D. E., Koski, A. T., & Phillips, M. M. 1976, ApJ, 206, 898

Peterson, B. M., Ferrarese, L., Gilbert, K. M., Kaspi, S., Malkan, M. A., Maoz, D., Merritt, D., Netzer, H., Onken, C. A., Pogge, R. W., Vestergaard, M., & Wandel, A. 2004, ApJ, 613, 682

Piconcelli, E., Bianchi, S., Miniutti, G., Fiore, F., Guainazzi, M., Jimenez-Bailon, E., & Matt, G. 2008, A&A, 480, 671

Porquet, D., & Dubau, J. 2000, A&AS, 143, 495

Pounds, K. A. 1990, MNRAS, 242, 20

Reeves, J. N., & Turner, M. J. L. 2000, MNRAS, 316, 234

Reeves, J. N., O'Brien, P. T., & Ward, M. J. 2003, ApJ, 593, L65

Reeves, J. N., Sambruna, R. M., Braito, V., & Eracleous, M. 2009b, ApJ, 702, L187

Reynolds, C.S. 1997, MNRAS, 286, 513

Risaliti, G. et al. 2009, MNRAS, 393, L1

Ross, R. R., Fabian, A. C., & Young, A. J. 1999, MNRAS, 306, 461

Ross, R. R., & Fabian, A. C. 2005, MNRAS, 358, 211

Rudy, R. J., & Tokunaga, A. T. 1982, ApJ, 256, L1

Sambruna, R. M., George, I. M., Mushotzky, R. F., Nandra, K., & Turner, T. J. 1998, ApJ, 495, 749

Sambruna, R. M., Eracleous, M., & Mushotzky, R. F. 1999, ApJ, 526, 60

Sambruna, R. M., Reeves, J. N., & Braito, V. 2007, ApJ, 665, 1030

Sambruna, R. M., Reeves, J. N., Braito, V., Lewis, K. T., Eracleous, M., Gliozzi, M., Tavecchio, F., Ballantyne, D. R., Ogle, P. M., & Tueller, J. 2009, ApJ, 700, 1473

Smith, R. A. N., Page, M. J., & Branduardi-Raymont, G. 2007, A&A, 461, 135

Smith, R. K., Brickhouse, N.S., Liedahl, D.A., & Raymond, J.C. 2001, ApJ, 556, L91

Spergel, D. N., et al. 2003, ApJS, 148, 175

Steenbrugge, K. C., Kaastra, J. S., Crenshaw, D. M., Kraemer, S. B., Arav, N., George, I. M., Liedahl, D. A., van der Meer, R. L. J., Paerels, F. B. S., Turner, T. J., & Yaqoob, T. 2005, A&A, 434, 569

Tombesi, F., Cappi, M., Reeves, J.N., Palumbo, G.G.C., Yaqoob, T., Braito, V., & Dadina, M. 2010, A&A, accepted (arXiv:1006.2858)

Tombesi, F., Sambruna, R., Reeves, J.N., Braito, V., Ballo, L., Gofford, J., Cappi, M., & Mushotzky, R. 2010b, ApJ, accepted

Torresi, E., Grandi, P., Guainazzi, M., Palumbo, G. G. C., Ponti, G., & Bianchi, S. 2009, A&A, 498, 61

Torresi, E., Grandi, P., Longinotti, A., Guainazzi, M., Palumbo, G. G. C., Tombesi, F., & Nucita, A. 2010, MNRAS, 401, 10

Tueller, J., et al. 2010, ApJS, 186, 378

Turner, T. J., & Pounds, K. A. 1989, MNRAS, 240, 833

Turner, T. J., George, I. M., Nandra, K., & Mushotzky, R. F. 1997, ApJ, 488, 164

Turner, T. J., & Miller, L. 2009, A&ARv, 17, 47

Urry, M., & Padovani, P. 1995, PASP, 107, 903

Vaughan, S., & Uttley, P. 2008, MNRAS, 390, 421

Wandel, A., Peterson, B. M., & Malkan, M. A. 1999, ApJ, 526, 579

This preprint was prepared with the AAS LaTeX macros v5.2.

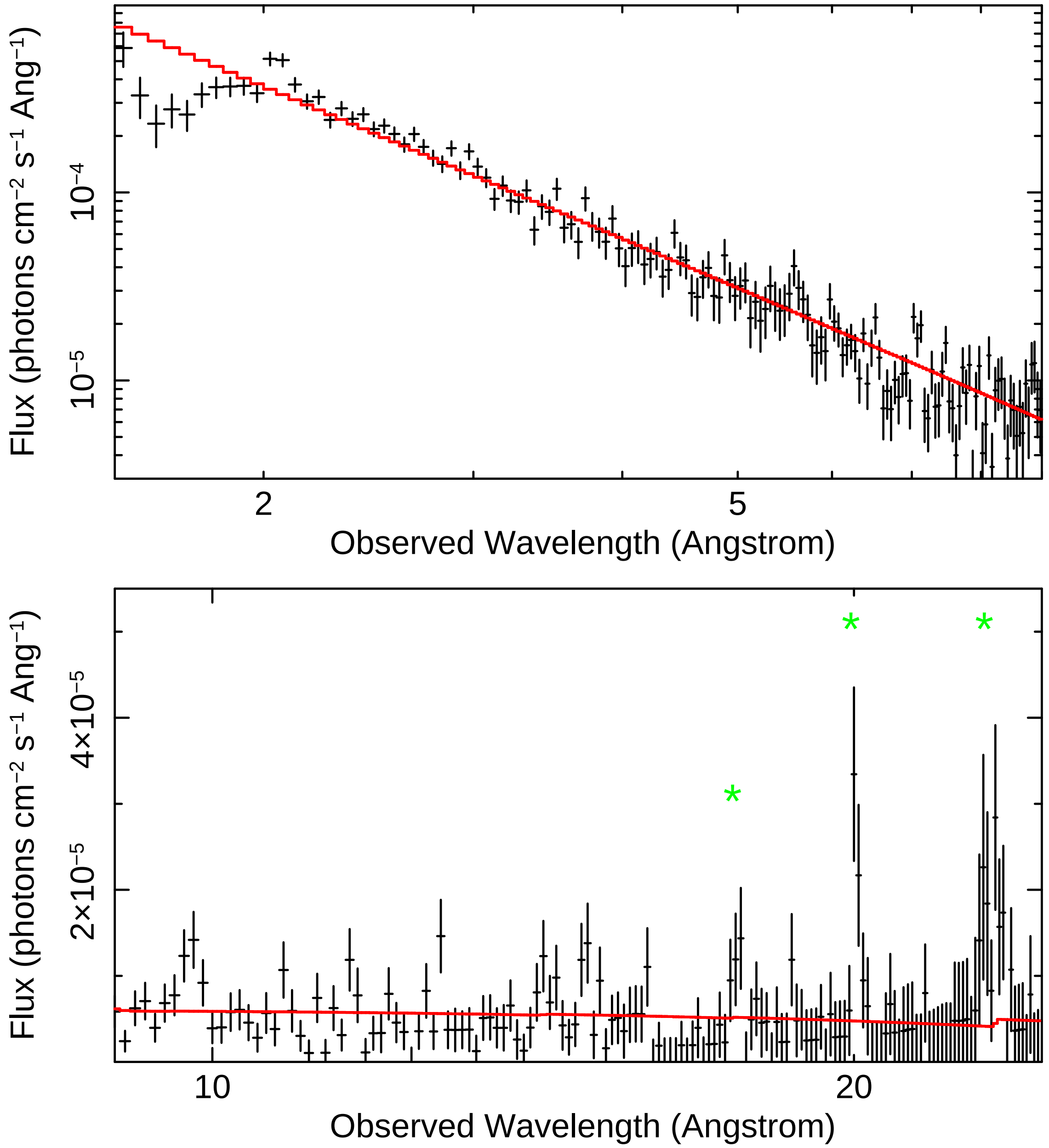

Fig. 1.— The Chandra LETG spectrum of 3C 445, showing the hard X-ray (top) and soft X-ray regions (lower) against observed–frame wavelength. The fluxed spectrum (black crosses) is plotted against a broken power-law continuum (solid line) for reference. The spectrum shortwards of 9Å ($> 1.4\,\mathrm{keV}$) is very hard, rising with energy (decreasing wavelength) with a photon index of $\Gamma = -0.64$, indicative of a highly absorbed continuum. Note the emission and absorption present at iron K. In the soft X-ray band several emission lines appear to be present. The star symbols denote the expected positions of (from right to left) the O VII He-α (forbidden or intercombination), O VIII Lyman-α and the O VII radiative recombination emission.

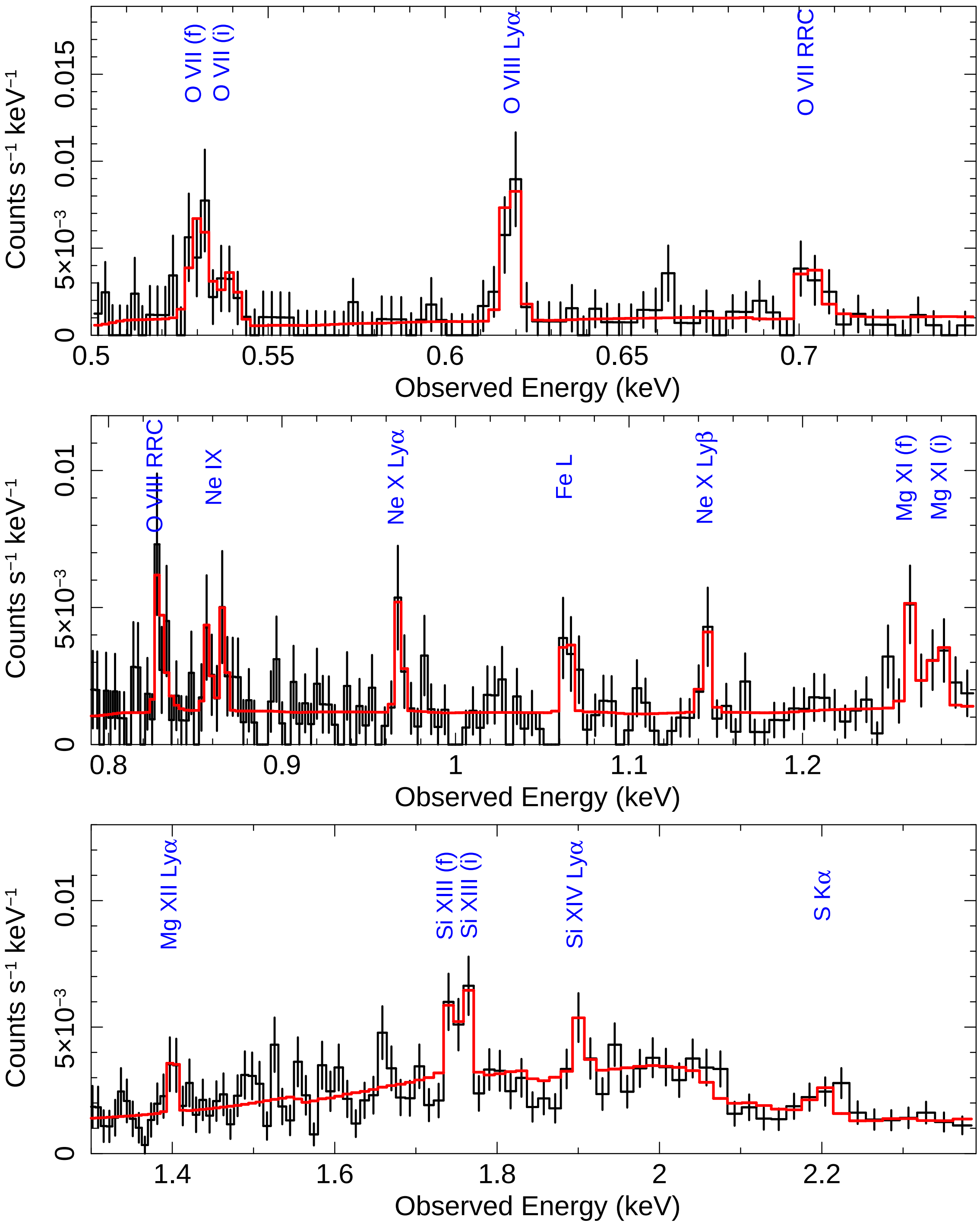

Fig. 2.— Chandra LETG spectra of 3C 445 showing several soft X-ray emission lines from O, Ne, Mg, Si and Fe L. The solid line represents the best-fit absorbed continuum model with Gaussian emission lines, as described in Section 3.2 and Tables 1 and 2.

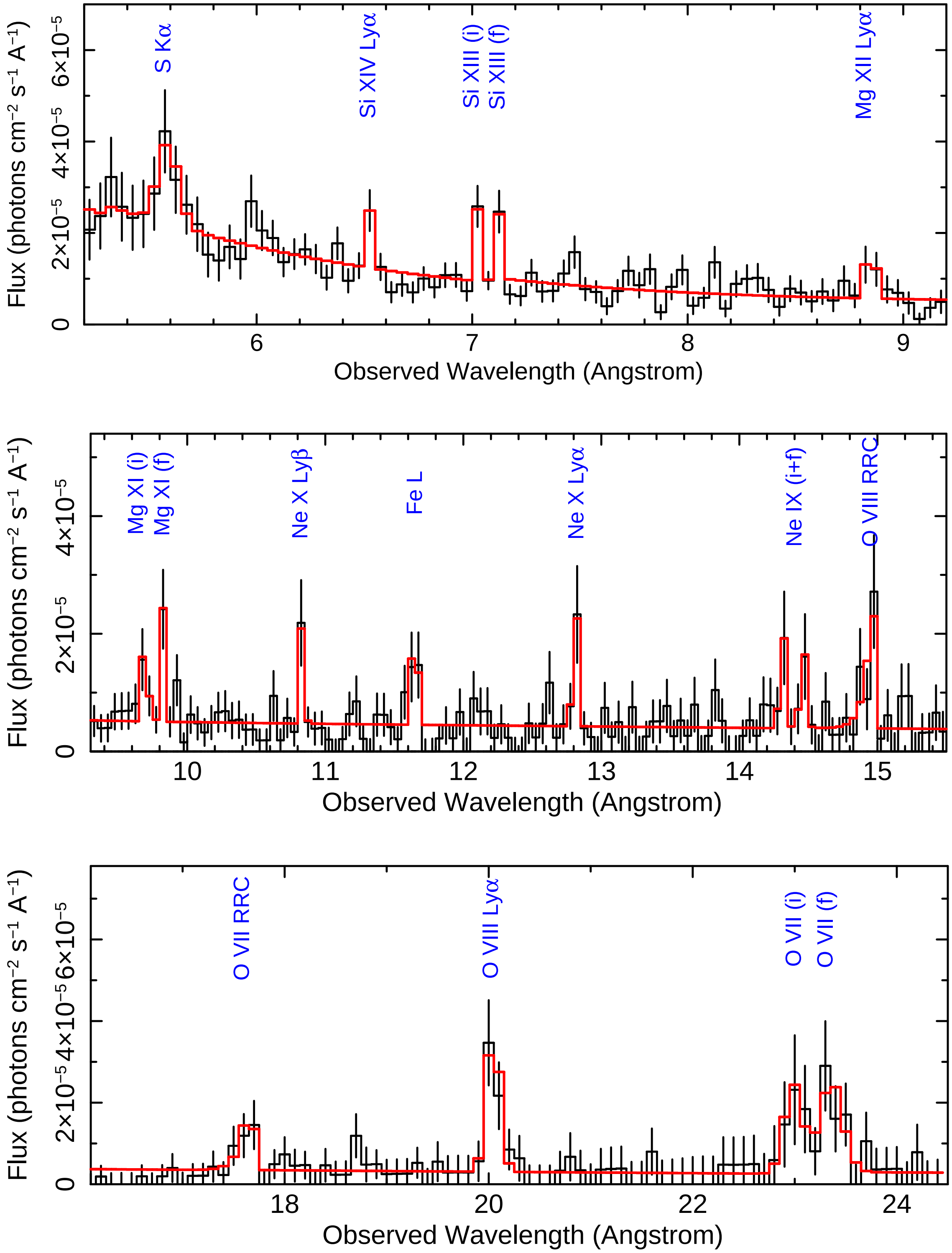

Fig. 3.— Fluxed LETG spectrum, plotted against observed–frame wavelength (in Angstroms). The solid line shows the same line model as plotted in Figure 2.

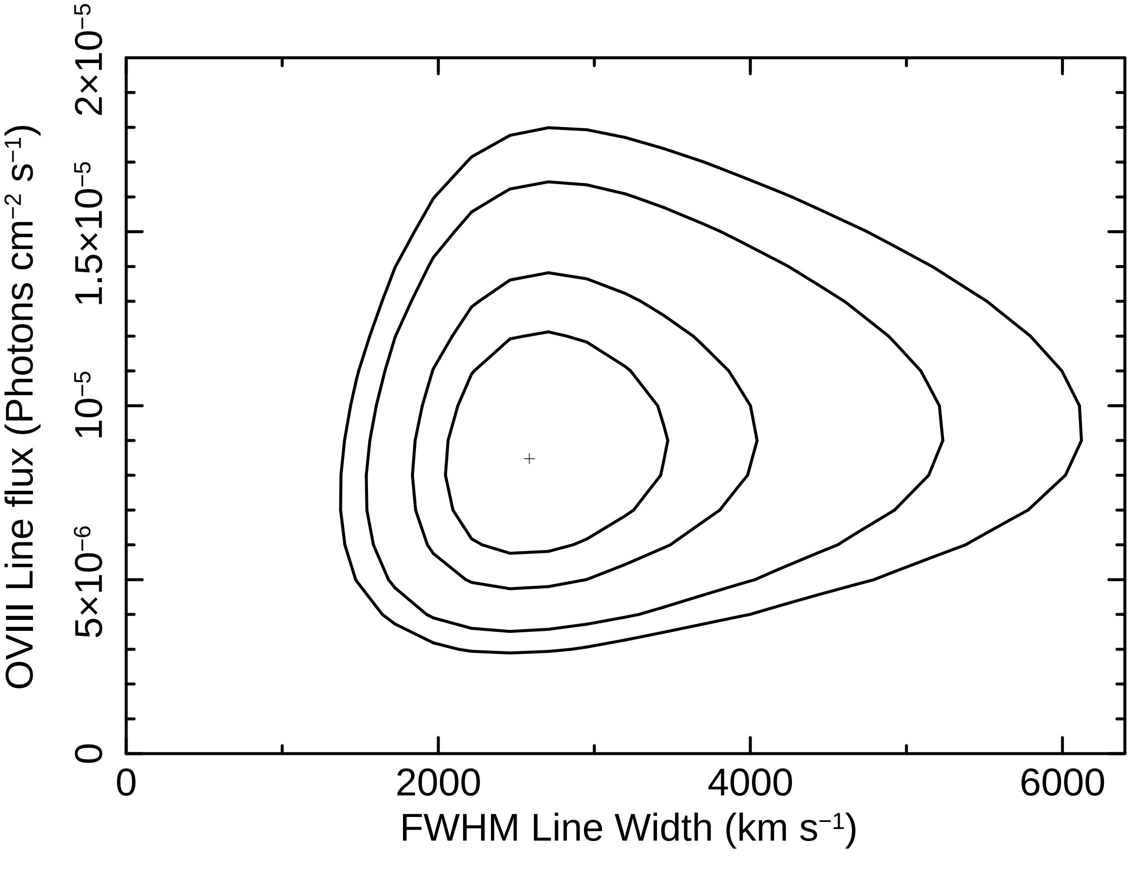

Fig. 4.— FWHM velocity width, fitted jointly to the O VII forbidden/intercombination and O VIII Lyman-α lines, plotted against O VIII Lyman-α line flux. The contours represent the 68%, 90%, 99% and 99.9% confidence levels for 2 parameters of interest.

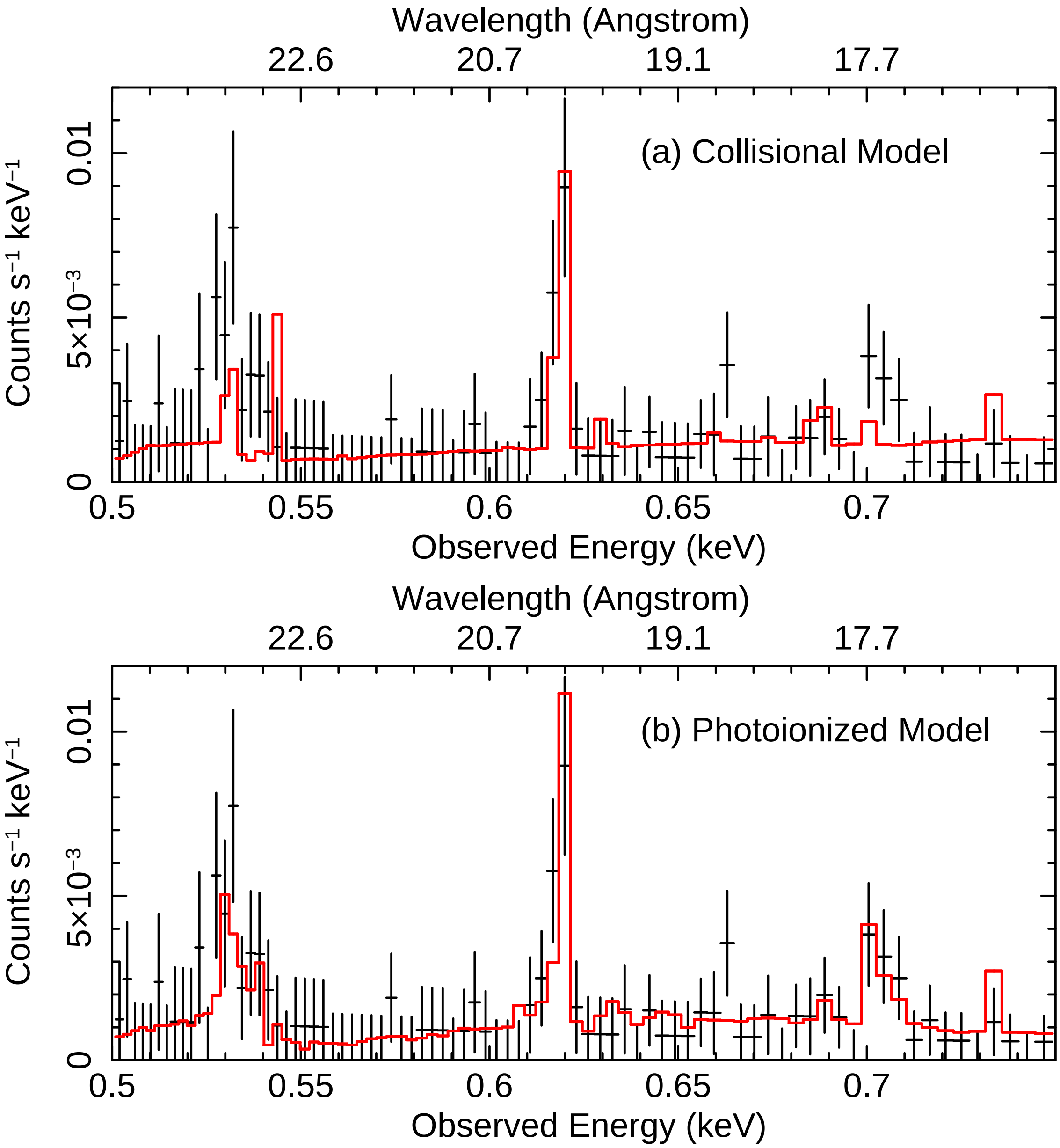

Fig. 5.— Comparison between (a) the collisionally ionized APEC emission model and (b) the photoionized XSTAR emission model in the Oxygen band, as discussed in Section 4.

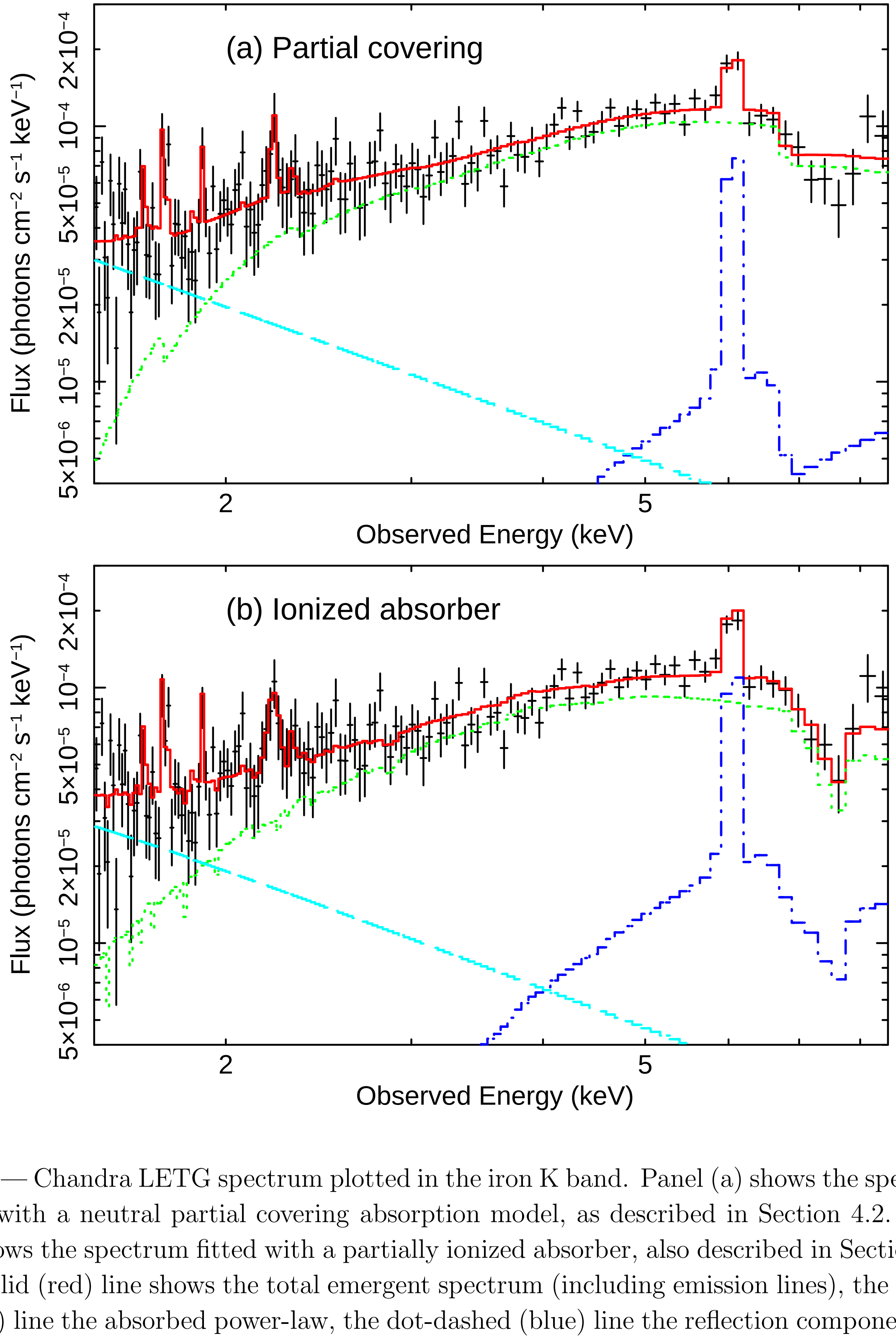

Fig. 6.— Chandra LETG spectrum plotted in the iron K band. Panel (a) shows the spectrum fitted with a neutral partial covering absorption model, as described in Section 4.2. Panel (b) shows the spectrum fitted with a partially ionized absorber, also described in Section 4.2. The solid (red) line shows the total emergent spectrum (including emission lines), the dotted (green) line the absorbed power-law, the dot-dashed (blue) line the reflection component and the dashed (cyan) line the unabsorbed scattered power-law. Note that the partially ionized absorber gives a better fit in the iron K band.

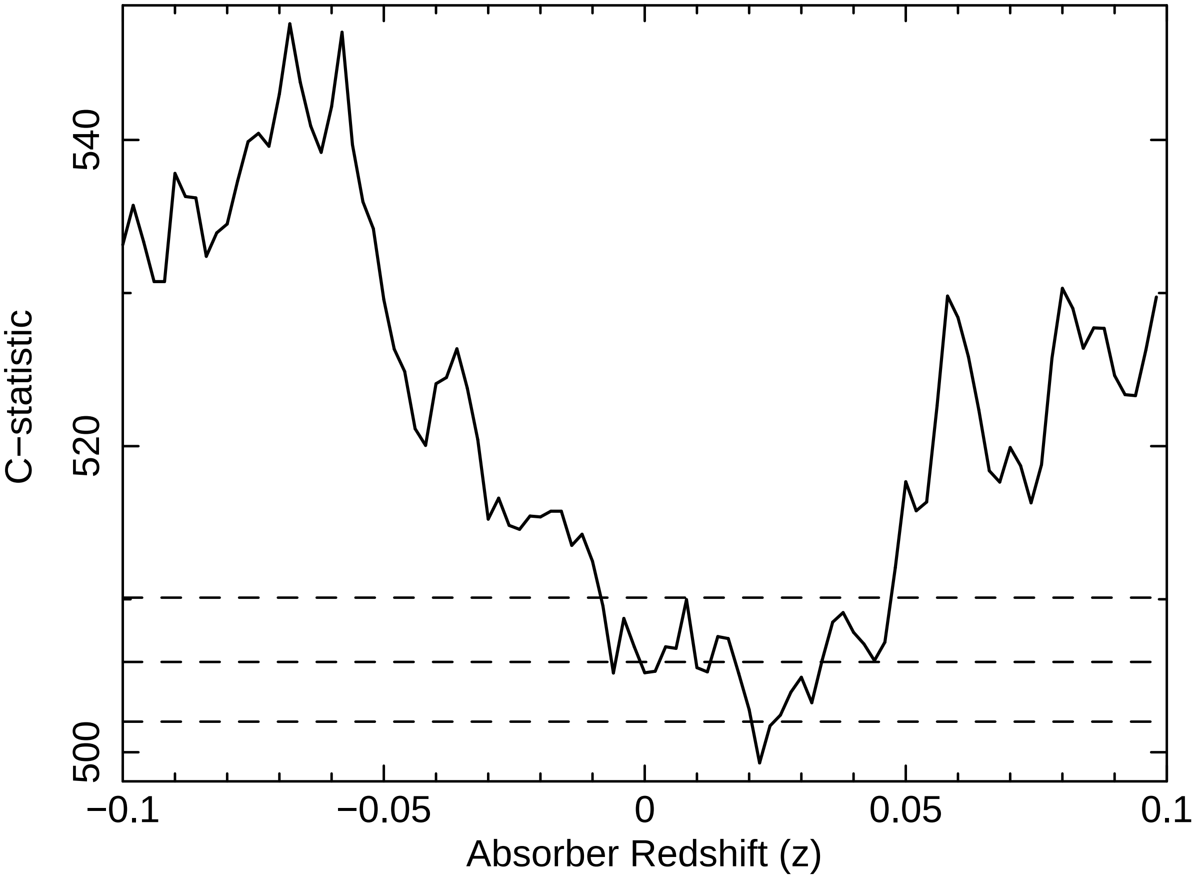

Fig. 7.— Overall fit statistic (C-statistic) plotted against absorber redshift (solid line). An absorber coincident with the redshift of 3C 445 at $z = 0.056$ appears to be ruled out at $> 99.9\%$ confidence level. Note the dashed horizontal lines represent (from bottom to top) the 90%, 99% and 99.9% confidence levels, for 1 interesting parameter. The best-fit absorber redshift of $z = 0.022 \pm 0.002$ implies that the absorber has a net blueshift of $-10000\,\mathrm{km\,s^{-1}}$, in the rest frame of 3C 445.

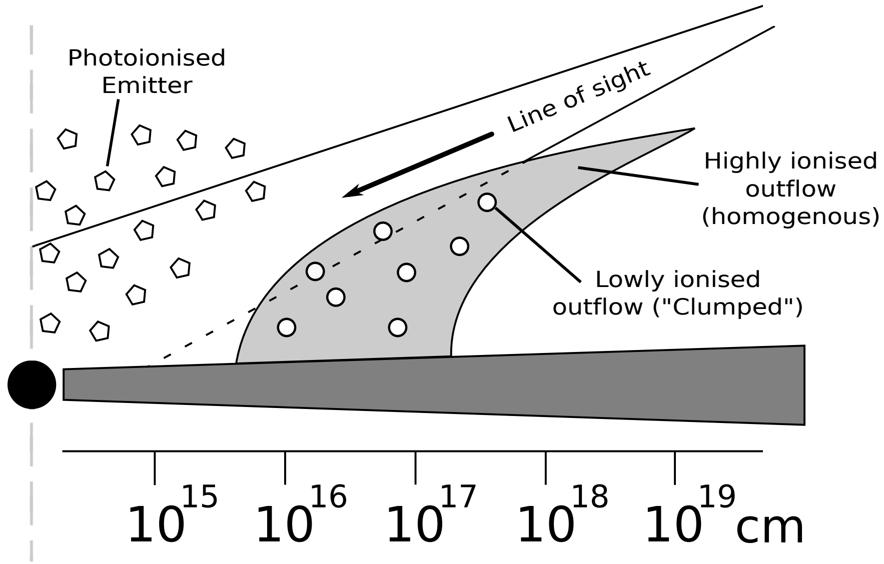

Fig. 8.— Schematic diagram showing the possible inner geometry of 3C 445. The line of sight towards the observer is represented by the solid and dashed black lines, while the grey dashed vertical line represents the direction of the radio-jet axis. In 3C 445 the line of sight towards the direct X-ray emission from the innermost region (black dashed line) is obscured by the outflowing matter, which may be in the form of a clumpy accretion disk wind. The observer has an unobscured view of the photoionized emission line clouds, which are responsible for the soft X-ray line emission. This highly ionized gas can also scatter continuum X-rays into the line of sight.

Table 1. Summary of LETG emission line parameters.

$E_{\rm rest}$ (eV)	$\lambda_{\rm rest}$ (Å)	Line Flux[a]	σ or kT (eV)[b]	EW (eV)	ΔC[c]	Line ID	$E^{d}_{\rm lab}$ (eV)
564.6 ± 2.6	21.98 ± 0.10	$18.8^{+7.6}_{-6.2}$	$6.3^{+2.8}_{-1.8}$	105^{+42}_{-35}	55.0	O VII Heα	561.1(f)
653.4 ± 1.0	18.99 ± 0.03	$8.3^{+4.0}_{-3.0}$	$2.0^{+1.2}_{-0.9}$	62^{+29}_{-22}	54.4	O VIII Lyα	653.7
740.2 ± 1.4	16.76 ± 0.03	$3.2^{+2.4}_{-1.7}$	$3.5^{+3.6}_{-1.9}$	31^{+22}_{-15}	18.8	O VII RRC	739.3
873.8 ± 1.4	14.20 ± 0.02	$2.2^{+1.5}_{-1.1}$	$3.0^{+4.0}_{-2.0}$	21^{+12}_{-10}	19.6	O VIII RRC	871.4
913 ± 5	13.59 ± 0.07	$2.6^{+1.6}_{-1.3}$	$7.2^{+4.0}_{-2.0}$	25^{+15}_{-12}	14.6	Ne IX Heα	905.1(f)
1022^{+1}_{-2}	$12.14^{+0.01}_{-0.02}$	$1.3^{+1.0}_{-0.8}$	< 4.0	19^{+15}_{-12}	14.2	Ne X Lyα	1022
1124 ± 2	11.04 ± 0.02	$1.2^{+0.9}_{-0.7}$	—	20^{+14}_{-12}	11.8^{e}	Fe XXIII	1125
1209^{+3}_{-2}	$10.26{\pm}^{+0.03}_{-0.02}$	$0.9^{+0.8}_{-0.6}$	—	18^{+16}_{-12}	10.7^{e}	Ne X Lyβ	1211
1341 ± 7	9.25 ± 0.05	$2.6^{+1.2}_{-1.0}$	$14.5^{+9.0}_{-5.0}$	59^{+27}_{-23}	26.1	Mg XI Heα	1331(f)
1480 ± 3	8.38 ± 0.02	$0.8^{+0.6}_{-0.5}$	< 21	21^{+16}_{-13}	10.2^{e}	Mg XII Lyα	1472
1853 ± 6	6.97 ± 0.02	$1.4^{+0.6}_{-0.5}$	$10.5^{+5.5}_{-4.0}$	32^{+14}_{-11}	23.7	Si XIII Heα	1839(f)
2010^{+6}_{-10}	$6.17^{+0.02}_{-0.03}$	$0.7^{+0.5}_{-0.4}$	< 13	13^{+16}_{-9}	9.5^{e}	Si XIV Lyα	2006
2343^{+16}_{-9}	$5.30^{+0.04}_{-0.02}$	$2.5^{+1.5}_{-1.3}$	< 38	43^{+25}_{-22}	11.5^{e}	S I Kα	2307
6364^{+40}_{-43}	1.95 ± 0.01	$22.9^{+6.6}_{-6.1}$	< 145	191^{+55}_{-51}	55.6	Fe I Kα	

[a] Measured Flux in units of 10^{-6} photons cm^{-2} s^{-1}

[b] 1σ Width of Gaussian line or temperature of radiative recombination continua (in eV). If only an upper-limit to the width is determined, the width has been fixed at $\sigma = 1\,{\rm eV}$ in the model.

[c] Improvement in C to fit after adding emission line component

[d] Expected line energy of transition taken from http://physics.nist.gov.

[e] ine detection significance at lower than 99.9% confidence.

Table 2. Summary of He-like Triplets

$E_{\rm rest}$ (eV)	$\lambda_{\rm rest}$ (Å)	Line Flux[a]	σ (eV)[b]	EW (eV)	ΔC[c]	Line ID[d]	$E_{\rm lab}$ (eV)
560.7 ± 1.4	22.13 ± 0.06	$8.6^{+4.7}_{-3.7}$	$2.4^{+2.8}_{-0.8}$	27^{+23}_{-12}	35.2	O VII(f)	561.1
569.5 ± 1.6	21.79 ± 0.06	$9.2^{+7.2}_{-4.1}$	–	21^{+20}_{-11}	16.0	O VII(i)	568.7
905.4 ± 2.3	13.70 ± 0.03	$1.0^{+1.0}_{-0.7}$	< 5	8^{+10}_{-6}	6.5[e]	Ne IX(f)	905.1
914.8 ± 2.0	13.56 ± 0.03	$1.2^{+1.0}_{-0.7}$	–	13^{+21}_{-10}	9.0[e]	Ne IX(i)	914.8
1334^{+2}_{-3}	$9.30^{+0.01}_{-0.02}$	$1.1^{+0.7}_{-0.5}$	< 21	19^{+12}_{-9}	16.4	Mg XI(f)	1331
1351^{+6}_{-3}	$9.18^{+0.04}_{-0.02}$	$0.8^{+0.7}_{-0.5}$	–	15^{+13}_{-9}	9.7	Mg XI(i or r)	1343 or 1352
1842^{+4}_{-5}	6.74 ± 0.02	$0.8^{+0.5}_{-0.4}$	< 6	16^{+10}_{-8}	12.0	Si XIII(f)	1839
1861 ± 3	6.67 ± 0.01	$1.1^{+0.5}_{-0.4}$	–	25^{+11}_{-9}	20.0	Si XIII(i or r)	1854 or 1865

[a] Measured Flux in units of 10^{-6} photons cm^{-2} s^{-1}

[b] ine widths, assuming the widths of the forbidden and intercombination lines are set to be equal for any single ion.

[c] Improvement in C to fit after adding emission line component

[d] Forbidden, intercombination and resonance lines denoted by f, i and r. Expected Lab–frame line energies in parenthesis in eV.

[e] ine detection significance at lower than 99% confidence.

Table 3. Summary of LETG Model parameters.

Model Component	Fit Parameter	Value	ΔC
1. Power-law continuum	Γ	$1.73^{+0.22}_{-0.19}$	
	normalization^{a}	$3.0 \pm 0.8 \times 10^{-3}$	
2. Scattered power-law	Γ	1.73 (tied)	57.0
	normalization^{a}	$6.6 \pm 1.0 \times 10^{-5}$	
3. Galactic absorption	$N_{\mathrm{H}}^{Gal\,b}$	$(1.5^{+0.6}_{-0.5}) \times 10^{21}$	
4. Ionized reflection	$\log \xi_{\mathrm{refl}}{}^{c}$	< 1.65	96.5
	normalization^{a}	$(2.49^{+0.83}_{-0.62}) \times 10^{-5}$	
5. Photoionized emission	$N_{\mathrm{H}}{}^{b}$	$10^{22\,f}$	125.6
	$\log \xi^{c}$	$1.82^{+0.13}_{-0.33}$	
	Mg abund	$2.6^{+2.6}_{-1.5}$	
	Si abund	$6.5^{+9.95}_{-3.86}$	
	outflow velocity^{d}	$+150^{+240}_{-210}$	
	normalization^{e} (k)	$(2.4^{+0.7}_{-0.6}) \times 10^{-6}$	
Second emission region	$\log \xi^{c}$	3.0 ± 0.4	10.0
	normalization^{e} (k)	$1.2^{+1.9}_{-0.9} \times 10^{-5}$	
6. Photoionized Absorber	$N_{\mathrm{H}}{}^{b}$	$(1.85^{+0.09}_{-0.11}) \times 10^{23}$	383.5
	$\log \xi^{c}$	$1.42^{+0.20}_{-0.12}$	
	blueshift	$-0.034 \pm 0.002c$	22.3
	outflow velocity^{d}	-10200 ± 600	
7. Fit statistic	C	498.4/450 d.o.f	

[a] Normalisation corresponds to flux measured at 1 keV, in units of photons $\mathrm{cm^{-2}\,s^{-1}\,keV^{-1}}$

[b] Column density in units of $\mathrm{cm^{-2}}$.

[c] Units of ionization parameter (ξ) in $\mathrm{erg\,cm\,s^{-1}}$.

[d] Units $\mathrm{km\,s^{-1}}$.

[e] Units of Xstar emission normalization factor (k) in units of $10^{38}\,\mathrm{erg\,s^{-1}\,kpc^{-2}}$.

[f] Model parameter fixed in fit.